

Article

Petrogenesis and Tectonic Implications of the Early Cretaceous Granitic Pluton in the Sulu Orogenic Belt: The Caochang Granitic Pluton as an Example

Yuanku Meng ^{1,2,3}, Zhongbo Wang ^{2,4,*}, Baoping Gan ⁵ and Jinqing Liu ^{1,2}

¹ College of Earth Science and Engineering, Shandong University of Science and Technology, Qingdao 266590, China; myk@sdust.edu.cn (Y.M.); jinqingliu@hotmail.com (J.L.)

² Laboratory for Marine Mineral Resources, Qingdao National Laboratory for Marine Science and Technology, Qingdao 266071, China

³ Key Laboratory of Deep-Earth Dynamics of Ministry of Natural Resources, Beijing 100037, China

⁴ Qingdao Institute of Marine Geology, China Geological Survey, Qingdao 266071, China

⁵ Department of Geology, Northwest University, Xi'an 710069, China; gannwu@163.com

* Correspondence: wangzhongbo@mail.cgs.gov.cn

Received: 22 April 2020; Accepted: 8 May 2020; Published: 11 May 2020



Abstract: The Sulu orogenic belt is the source of information on important magmatic events associated with the collision of the Yangtze craton and North China craton (NCC) and the destruction of the NCC during the Mesozoic in eastern China. In this study, we have, for the first time, identified a monzonitic granitic pluton. We hereby present petrological, geochemical, and zircon U-Pb-Hf-O isotopic data, shedding new light on the petrogenesis and tectonic implications for the granitic pluton in the Sulu belt. LA-ICP-MS and SHRIMP II analyses of zircon grains suggest that the monzonitic granitic pluton was crystallized in the Early Cretaceous (ca. 120 Ma). Geochemically, the granitic pluton shows sub-alkaline, high-K calc-alkaline, and metaluminous signatures, and is genetically of I-type granite, excluding the possibility of S-type granite, as evidenced by mantle-like zircon oxygen isotopic features. In addition, the pluton is enriched in light REE and large-ion lithophile elements (LILE) (e.g., La, Cs, Ba, K, and Pb), but depleted in high-field-strength elements (HFSE) (e.g., Nb, Ta, P, and Ti), suggesting an arc-related affinity. Zircon Hf isotopes ($\epsilon_{\text{Hf}}(t) = -27.51 \sim -32.35$; $T_{\text{DM2}} = 2979 \sim 3175$ Ma) and mantle-like $\delta^{18}\text{O}$ values (5.12–6.24‰) together indicate that the identified granitic pluton is derived from the partial melting (reworking) of the ancient mafic lower crustal material, with no supra-crustal material participation. Moreover, high Magnesium number ($\text{Mg\#} = 42\text{--}49$) values and mafic micro-granular enclaves suggest that mantle-derived magma participated in the evolution of the granitic pluton in this study. Integrating the findings of this study and previous work, we propose that the Caochang granitic pluton is derived from the partial melting of the deep Yangtze basaltic lower crust during the Early Cretaceous, and that the large-scale thinning of the lithospheric mantle was the main factor that led to Early Cretaceous magmatic flare-up in the Sulu orogenic belt.

Keywords: Sulu orogenic belt; Hf-O isotopes; Early Cretaceous; Yangtze lower crust; crust-mantle interaction

1. Introduction

The Sulu orogenic belt is an ideal place for studying continental deep subduction and the crust–mantle interaction [1–7]. Multiple studies have reported that the Sulu orogenic belt experienced two stages of evolution, namely the deep-subduction stage and the subsequent exhumation stage [4,8,9]. In addition, multiple geodynamic scenarios have been constructed in the Sulu belt [1,2,10–13]. Early Cretaceous granitoid rocks (130–110 Ma), which are widely distributed throughout the Sulu orogenic

belt, have been regarded as post-collisional products [4,5,11,14,15]. Competing models were proposed to explain the petrogenesis of the Early Cretaceous granitoid rocks in the Sulu belt [16–20]. Niu [19] and Gao [20] proposed that the granites were most probably derived from anatexis of the continental lower crust (ca. 20–25% partial melting of the mafic granulite), and further pointed out that the stagnant paleo-Pacific slab beneath the subcontinental lithospheric mantle was the main inducing factor that brought about convective asthenosphere, leading to lower crustal partial melting. However, Dai [21] and Wang [12] argued that rollback of the western paleo-Pacific slab caused the strongest mantle perturbation, resulting in large-scale partial melting and strong Early Cretaceous (130–110 Ma) magmatic events in the Dabie–Sulu orogenic belt and other regions of eastern China. In addition to above models, Ling [22] argued that Early Cretaceous magmatism was related to ridge subduction, and stressed that the ridge subduction was key driving force leading to the destruction of the North China craton (NCC) in ca. 125 Ma. Additionally, the magma sources of Early Cretaceous granites are in dispute. Yan [23] and Zhao [5] concluded that the granites were produced by partial melting of upper continental crust, while Gao [20] argued that granites were products of lower continental crust with injection of mantle magma, and reported that upper crustal material played a minor or negligible role. Together with zircon oxygen isotopes ($\delta^{18}\text{O}$), Meng [11] considered the felsic rocks to be the products of melting of deep crustal material which did not experience high-temperature water–rock interactions. With regard to the magma source, it was proved that granites from the Sulu belt were products of partial melting of the Yangtze crust [4,18,24,25]. According to a recent new study, the under-thrust lower crust of the Yangtze was the source for the granites in both the Jiaobei terrane (akin to the NCC affinity) and the Sulu belt [26]. This study challenged traditional notions, and implied that crustal material of the NCC was not the sole source of Late Jurassic to Early Cretaceous granites in the Jiaobei terrane. In order to evaluate related debates and issues, we identified a new granitic outcrop (artificial exposure—a quarry) in order carry out new petrological, geochronological, and geochemical studies for the first time in the central segment of the Sulu belt. Based on these datasets, we discuss its petrogenesis and the geodynamic scenario, and evaluate the tectonic setting of granites in the study area.

2. Regional Geological Setting and Petrological Features

Owing to the left-lateral movement of the Tanlu fault in the Early Jurassic, the Dabie–Sulu orogenic belt was separated into two parts, the Sulu belt to the east and Dabie belt to the west (Figure 1a). According to regional faults and mélangé, the Sulu belt is bound by the Jiashan–Xiangshui fault (JXF) to the south and by the Baichihe (Wulian)–Qingdao–Yantai fault (WQYF) to the north [27,28]. Furthermore, Liu [3] proposed that the whole Sulu orogenic belt could be divided into the ultra-high pressure (UHP) and high-pressure (HP) sub-zones that are characterized in the Shuyang–Jinping suture zone. The UHP and HP rocks experienced widely retrograde metamorphism (amphibolite facies), and subsequently were intruded upon by Late Jurassic–Early Cretaceous granites [3] (Figure 1b). It is accepted that the framework of the Dabie–Sulu orogenic belt was well constructed. According to metamorphism and magmatism in the Dabie–Sulu belt, four important stages were recognized: (1) Continental deep subduction in the Triassic between the Yangtze and north China craton (ultra-high pressure magmatism); (2) Syn-exhumation anatexis in the Late Triassic (syn-exhumation magmatism); (3) Anatexis of the thickened crust in the Late Jurassic (post-collisional magmatism); and (4) Anatexis of orogenic crust in the Early Cretaceous (post-collisional magmatism) [1,2,4,8,10,14]. The four stages correspond with three different magmatic activities in the Sulu belt [1,2,4,5,14,24,25,29], with the stages containing: (1) 225–205 Ma; (2) 160–150 Ma; and (3) 130–110 Ma. The Late Triassic magmatic rocks, composed of granites and mafic complexes, only outcrop in the Shidao area. Geochemical and isotopic evidence suggests them to be related to syn-exhumation tectonism [14]. Compared to the Late Triassic magmatic rocks, the Late Jurassic magmatic rocks have more outcrops, which are mainly distributed in Rushan and Wendeng areas [24,25]. Multiple studies demonstrated that the Late Jurassic magmatic rocks were generated from partial melting of thickened continental crust [4]. The Early Cretaceous

magmatic activities were significantly sharp (magmatic flare-up), and cropped out throughout the Sulu orogenic belt [4,18]. Early Cretaceous magmatic rocks are generally considered to be products of the NCC destruction. The Late Jurassic and Early Cretaceous magmatism had a post-collisional background and was formed in the within-plate setting.

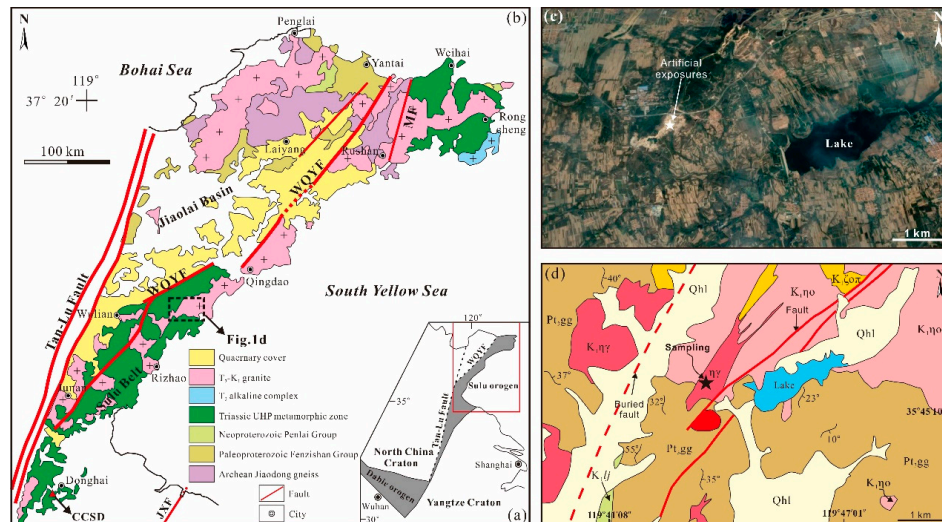


Figure 1. (a) Simplified tectonic framework of the Dabie–Sulu orogenic belt (from Yang [1,2] and Xu [14]). (b) Simplified geological map of the Sulu orogenic belt. (c) Modification of the Google Earth map. (d) Geological map of the study and adjacent areas (modified from 1:250,000 geological map of the PRC). WQYF: Wulian–Qingdao–Yantai fault; JXF: Jiashan–Xiangshui fault; MF: Milashan Fault; CCSD: China continental scientific drilling.

The study region, located in the middle segment of the Sulu belt, is adjacent to the village of Caochang. Thus, we denominated the newly identified pluton as Caochang granite (Figures 1c,d and 2a,b). Although the simplified map shows that the study region is characterized by granites and UHP rocks, the study region is covered by quaternary covers, as suggested by Google Earth and a field survey (Figures 1c and 2a). Therefore, new identified exposures could provide new clues to evaluate the debates, as described in the introduction. Using 1:50,000 and 1:250,000 mapping and a geological survey, the study region was found to be characterized by granitoid rocks and granitic gneisses (Figure 1d).

The newly identified pluton showed good artificial exposures (Figure 2a,b). We collected representative samples from the limited rock exposures for research. The field observations revealed that the granitic pluton showed typical magmatic structures, and few mafic micro-granular enclaves were found in the granitic pluton (Figure 2c). The granitic samples showed medium-grained and equigranular textures, mainly comprising euhedral K-feldspar (30~35%), plagioclase (~35%), biotite (~15%), and quartz (10~20%), as well as a small amounts of accessory minerals (~5%) (Figure 2d–f). Equivalent contents (volume) of plagioclase and K-feldspar suggested that the granitic pluton was composed of monzonitic granite. K-feldspar crystals were marked by earthy appearances and Carlsbad twinning, with few crystals showing envelope and sector-shaped twinning (Figure 2d,e). Plagioclase grains had typical zonal textures and polysynthetic twinning, and few crystals were subjected to sericite (Figure 2d,e). Compared to the host granite, the mafic micro-granular enclaves (MMEs) were crystallite textures marked by sub-euhedral to anhedral biotite, amphibole, and plagioclase crystals (Figure 2f–i). The MMEs had a clear boundary with the host pluton, and few sanidine crystals were identified near the contact boundary (Figure 2f). The sanidine crystals, which were marked by clear appearances, suggested a quenching process. Additionally, acicular apatite crystals also suggested a quick cooling process (Figure 2h). As such, feldspar and quartz megacrysts indicated a magma mixing process between the MME and host granite (Figure 2g,i).

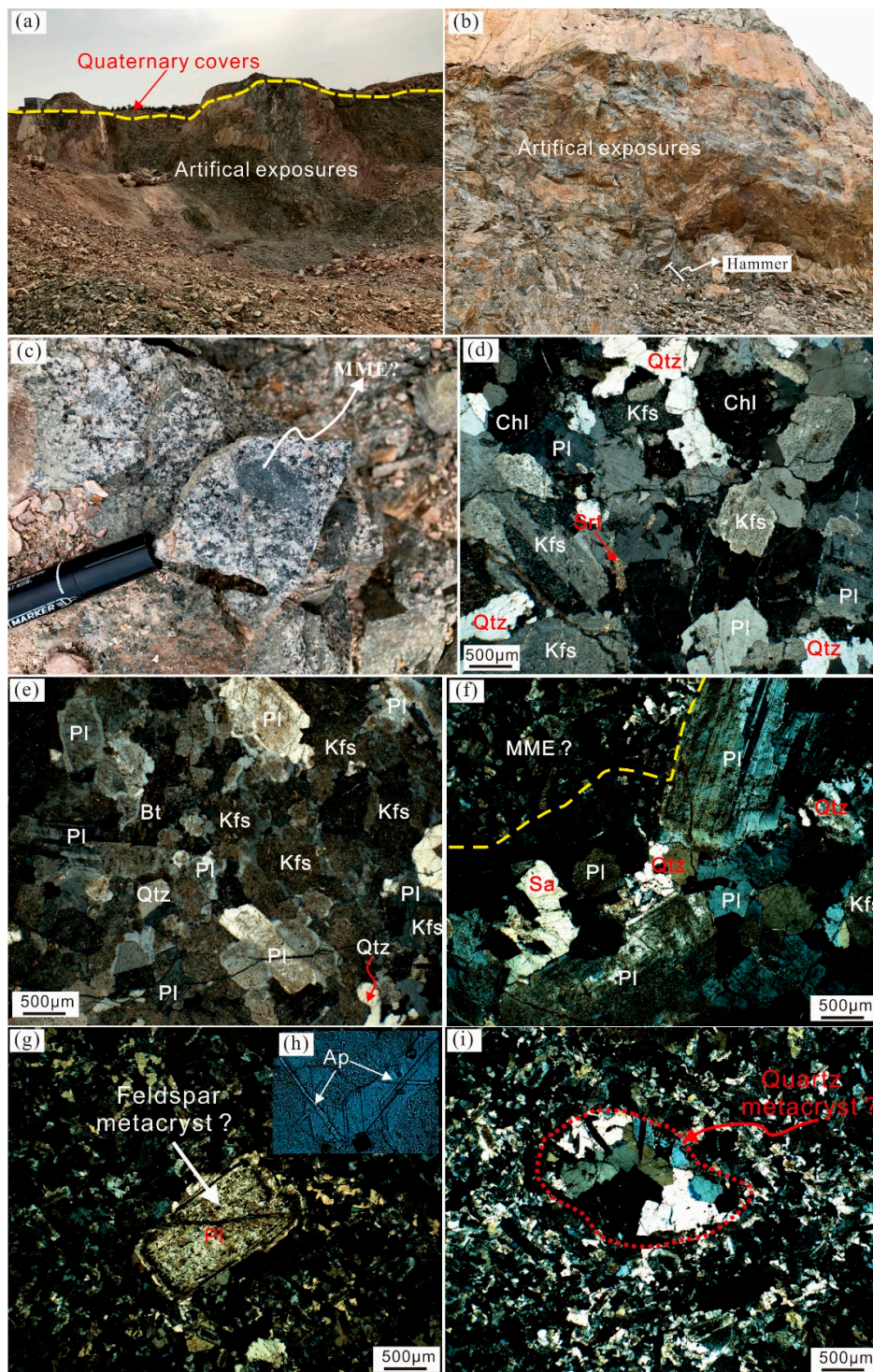


Figure 2. (a,b) Field artificial exposures of the identified granitic pluton. (c) Granitic rocks with the mafic micro-granular enclave. (d,e) Micro-structural textures of the identified granitic pluton. (f) The boundary of mafic micro-granular enclaves (MMEs) and host granite pluton. (g) Plagioclase metacryst of MME. (h) Acicular apatite crystal. (i) Quartz metacryst of MMEs.

Field observations and petrological-mineral analyses suggested that the granitic pluton was composed of monzonitic granite, corresponding to CIPW calculation results.

3. Methods

3.1. Zircon U-Pb Geochronology and Oxygen Isotope Analyses

Zircon separation and cathode luminescence (CL) images were undertaken at the Institute of Geology, Chinese Academy of Geological Sciences (Beijing, China). Zircon LA-ICP-MS U-Pb dating was completed at the Wuhan Sample Solution Analytical Technology Co., Ltd (Wuhan, China) using a GeolasPro laser ablation system comprising a COMPexPro 102 ArF excimer laser and a MicroLas optical system. In addition, ICP-MS (Agilent 7700e) was adopted to obtain ion signal intensities. During the experiment, helium (He) was applied as a carrier gas. Standard zircon 91500 and glass NIST610 were used to correct the U-Th-Pb isotope system and trace elements, respectively. Due to weak signals of ^{204}Pb and interference of ^{204}Hg , the traditional method could not be used to determine accurate contents of U and Pb. Therefore, we used Com Pb Corr#_315G software embedded in EXCEL to carry out common Pb corrections. The detailed analytical procedures and principles were described by Liu [30] and Zong [31]. Zircon SHRIMP II analyses were performed at the Institute of Geology, Chinese Academy of Geological Sciences. A primary O^{2-} ion beam of 3–6 nA was utilized to bombard the surface of zircons with a 20- μm spot size in diameter. The standard zircons 91500 (U = 91 ppm), SL13 (U = 238 ppm), and M257 (U = 840 ppm) were used to correct the U-Th-Pb isotope system. TEMORA, dated at ca. 417 Ma, was analyzed for calibration of $^{206}\text{Pb}/^{238}\text{U}$ ratios per three analyses. The related techniques and processes were described by Williams [32]. Zircon oxygen isotopes were also completed at the Institute of Geology, Chinese Academy of Geological Sciences (Beijing, China), using the SHRIMP II MC technique (Beijing SHRIMP Center, Beijing, China). Detailed oxygen isotopic procedures and analytical principles were described by Black [33].

3.2. Zircon Lu-Hf Isotopes

In situ Zircon Lu-Hf isotopes were obtained at the Wuhan Sample Solution Analytical Technology Co., Ltd. using a Neptune Plus MC-ICP-MS (Thermo Fisher Scientific, Germany) in combination with a Geolas HD excimer ArF laser ablation system. Helium (He) was used as the carrier gas within the ablation cell and was merged with argon (makeup gas) after the ablation cell. During the experiment, standard zircons GJ-1 (internal standard) and 91500 (external standard) were used to verify and correct measured data. The assayed Hf values were consistent with the recommended values within the uncertainty. Detailed analytical conditions and procedures, as well as processes, are described by Hu [34].

3.3. Major and Trace Whole-Rock Elements

Major and trace whole-rock element compositions were assayed at the Testing center of Shandong Bureau of China Metallurgical Geology Bureau (Jinan, China). Major elements were determined using the ARL 9900XP XRF technique, and trace elements were assayed by the ICP-MS method. The analytical uncertainties were controlled within 0.1–1% (RSD), and loss on ignition (LOI) was obtained by means of a 500- μg rock powder that was heated up to ~ 1100 °C for one hour. The precision of the ICP-MS was $\pm 10\%$, and some trace elements were found to represent $\pm 5\%$.

4. Results

4.1. Zircon U-Pb Dating Results

Three samples from the different exposures of the granitic pluton were selected for zircon U-Pb dating. Zircon CL images revealed that zircons from the investigated area showed prismatic crystal morphologies, with ratios of length and width ranging from 1:1 to 4:1 (Figure 3). High ratios of Th/U (>0.4) and clear zircon zonal textures suggested an igneous origin [35]. The zircon LA-ICP-MS and SHRIMP II U-Pb dating results are listed in Table 1.



Figure 3. Representative zircon CL images of the granitic pluton (red circle for the U-Pb dating field, yellow circle for Lu–Hf field, white dotted circle for the oxygen isotopic field).

In total, 19 and 26 spots were assayed using LA-ICP-MS for samples My121 and My122, respectively. Excluding a few dating spots, the My121 sample had ages of $^{206}\text{Pb}/^{238}\text{U}$ ranging from 113.9 ± 2.1 to 126.2 ± 3.2 Ma, with a weighted average age of 119.6 ± 1.8 Ma (MSWD = 2.7). The sample My122 yielded ages of $^{206}\text{Pb}/^{238}\text{U}$ varying from 114.3 ± 1.5 to 126.9 ± 2.4 Ma, with a weighted average age of 118.7 ± 1.3 Ma (MSWD = 2.2). In order to further address absolute emplacement age of the pluton, the third sample, My1211, which contained 14 effective spots, was analyzed using the SHRIMP II method. The analytical results suggested the absolute crystallization age of the pluton was ca. 121.9 ± 1.4 Ma (MSWD = 1.4). Figure 4 demonstrates that all the dating spots fell along the concordant curves, suggesting no radiogenic Pb losses.

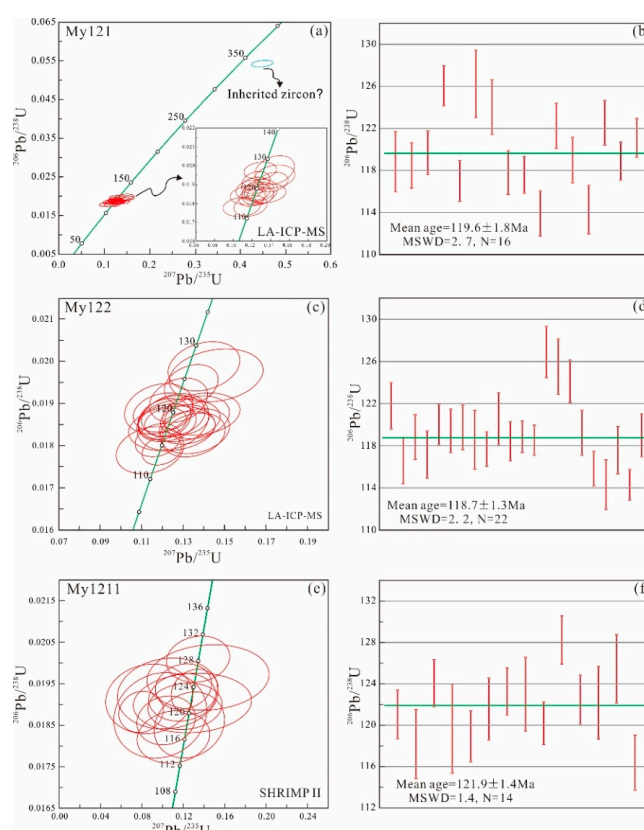


Figure 4. Zircon U-Pb concordia diagrams for the Caochang granitic pluton in the Sulu belt ((a–d) for the LA-ICP-MS technique, (e,f) for the SHRIMP II technique).

Table 1. Zircon U–Pb dating results of the granitic pluton in the study area.

| Spot Number | Th | U | Th/U | Ti Contents | °C | ²⁰⁷ Pb/ ²³⁵ U | | ²⁰⁶ Pb/ ²³⁸ U | | ²⁰⁶ Pb/ ²³⁸ U | | Methods |
|-------------|-----|-----|------|-------------|-----|-------------------------------------|---------|-------------------------------------|---------|-------------------------------------|-----|---------|
| | | | | | | Ratio | 1σ | Ratio | 1σ | Age (Ma) | 1σ | |
| My1-2-1-01 | 169 | 142 | 1.19 | 4.68 | 679 | 0.12810 | 0.01257 | 0.01860 | 0.00045 | 118.8 | 2.8 | I |
| My1-2-1-02 | 168 | 118 | 1.42 | 7.70 | 722 | 0.13558 | 0.01369 | 0.01855 | 0.00034 | 118.5 | 2.1 | I |
| My1-2-1-04 | 229 | 173 | 1.32 | 6.76 | 710 | 0.11745 | 0.00955 | 0.01874 | 0.00032 | 119.7 | 2.1 | I |
| My1-2-1-05 | 405 | 200 | 2.02 | 4.12 | 669 | 0.12890 | 0.01153 | 0.01975 | 0.00030 | 126.1 | 1.9 | I |
| My1-2-1-06 | 252 | 375 | 0.67 | 7.44 | 719 | 0.44894 | 0.01570 | 0.05428 | 0.00058 | 340.8 | 3.5 | I |
| My1-2-1-08 | 189 | 168 | 1.12 | 3.55 | 657 | 0.11994 | 0.00922 | 0.01832 | 0.00030 | 117.0 | 1.9 | I |
| My1-2-1-09 | 169 | 115 | 1.47 | 2.91 | 642 | 0.14438 | 0.01395 | 0.01978 | 0.00051 | 126.2 | 3.2 | I |
| My1-2-1-10 | 176 | 137 | 1.28 | 7.31 | 717 | 0.14420 | 0.01435 | 0.01943 | 0.00041 | 124.0 | 2.6 | I |
| My1-2-1-11 | 175 | 133 | 1.32 | 3.36 | 653 | 0.11603 | 0.01281 | 0.01844 | 0.00033 | 117.8 | 2.1 | I |
| My1-2-1-12 | 512 | 247 | 2.07 | 5.87 | 698 | 0.13140 | 0.00787 | 0.01841 | 0.00027 | 117.6 | 1.7 | I |
| My1-2-1-13 | 288 | 195 | 1.47 | 3.79 | 662 | 0.10897 | 0.01315 | 0.01783 | 0.00034 | 113.9 | 2.1 | I |
| My1-2-1-14 | 159 | 137 | 1.17 | 4.13 | 669 | 0.14210 | 0.01081 | 0.01914 | 0.00034 | 122.2 | 2.1 | I |
| My1-2-1-15 | 198 | 127 | 1.56 | 38.98 | 892 | 0.12686 | 0.01149 | 0.01863 | 0.00034 | 119.0 | 2.2 | I |
| My1-2-1-16 | 213 | 118 | 1.80 | 5.05 | 685 | 0.11850 | 0.01170 | 0.01789 | 0.00036 | 114.3 | 2.3 | I |
| My1-2-1-17 | 216 | 150 | 1.44 | 3.42 | 654 | 0.12453 | 0.00984 | 0.01919 | 0.00033 | 122.5 | 2.1 | I |
| My1-2-1-18 | 300 | 187 | 1.60 | 3.74 | 661 | 0.12557 | 0.00921 | 0.01861 | 0.00028 | 118.9 | 1.8 | I |
| My1-2-1-19 | 212 | 175 | 1.22 | 5.05 | 685 | 0.12392 | 0.01002 | 0.01896 | 0.00029 | 121.1 | 1.8 | I |
| My1-2-2-01 | 210 | 142 | 1.48 | 5.78 | 697 | 0.12784 | 0.00926 | 0.01907 | 0.00035 | 121.8 | 2.2 | I |
| My1-2-2-02 | 152 | 128 | 1.18 | 6.21 | 703 | 0.13503 | 0.01014 | 0.01825 | 0.00034 | 116.6 | 2.2 | I |
| My1-2-2-03 | 136 | 117 | 1.16 | 5.10 | 686 | 0.12819 | 0.01301 | 0.01860 | 0.00033 | 118.8 | 2.1 | I |
| My1-2-2-04 | 184 | 143 | 1.29 | 5.26 | 689 | 0.13567 | 0.01109 | 0.01834 | 0.00035 | 117.2 | 2.2 | I |
| My1-2-2-05 | 356 | 180 | 1.97 | 2.53 | 631 | 0.12047 | 0.00956 | 0.01878 | 0.00031 | 120.0 | 1.9 | I |
| My1-2-2-06 | 184 | 150 | 1.23 | 6.40 | 705 | 0.12527 | 0.01013 | 0.01870 | 0.00032 | 119.4 | 2.0 | I |
| My1-2-2-07 | 287 | 166 | 1.73 | 9.75 | 743 | 0.13883 | 0.01232 | 0.01875 | 0.00033 | 119.7 | 2.1 | I |
| My1-2-2-08 | 76 | 66 | 1.16 | 2.82 | 639 | 0.12512 | 0.01145 | 0.01856 | 0.00044 | 118.6 | 2.8 | I |
| My1-2-2-09 | 385 | 217 | 1.78 | 3.75 | 661 | 0.13204 | 0.00892 | 0.01842 | 0.00026 | 117.7 | 1.6 | I |
| My1-2-2-10 | 116 | 110 | 1.05 | 5.46 | 692 | 0.11826 | 0.01086 | 0.01887 | 0.00039 | 120.5 | 2.5 | I |
| My1-2-2-11 | 267 | 184 | 1.45 | 5.15 | 687 | 0.12233 | 0.00926 | 0.01854 | 0.00029 | 118.4 | 1.9 | I |
| My1-2-2-12 | 873 | 309 | 2.82 | 4.23 | 671 | 0.13081 | 0.00775 | 0.01861 | 0.00023 | 118.9 | 1.5 | I |
| My1-2-2-13 | 625 | 303 | 2.06 | 5.72 | 696 | 0.12159 | 0.00668 | 0.01856 | 0.00022 | 118.5 | 1.4 | I |
| My1-2-2-15 | 100 | 102 | 0.99 | 5.50 | 693 | 0.14010 | 0.01142 | 0.01988 | 0.00039 | 126.9 | 2.4 | I |
| My1-2-2-16 | 148 | 114 | 1.30 | 9.52 | 741 | 0.14599 | 0.01492 | 0.01966 | 0.00041 | 125.5 | 2.6 | I |
| My1-2-2-18 | 535 | 225 | 2.38 | 4.79 | 681 | 0.13395 | 0.00859 | 0.01944 | 0.00032 | 124.1 | 2.0 | I |
| My1-2-2-19 | 567 | 263 | 2.15 | 6.36 | 705 | 0.13667 | 0.01036 | 0.01867 | 0.00033 | 119.2 | 2.1 | I |
| My1-2-2-20 | 463 | 231 | 2.00 | 3.92 | 665 | 0.11782 | 0.00720 | 0.01813 | 0.00026 | 115.8 | 1.6 | I |
| My1-2-2-21 | 133 | 120 | 1.12 | 3.54 | 657 | 0.11409 | 0.01077 | 0.01789 | 0.00037 | 114.3 | 2.3 | I |
| My1-2-2-22 | 178 | 140 | 1.27 | 6.33 | 705 | 0.12465 | 0.01378 | 0.01841 | 0.00035 | 117.6 | 2.2 | I |
| My1-2-2-23 | 231 | 356 | 0.65 | 2.76 | 638 | 0.11978 | 0.00629 | 0.01789 | 0.00023 | 114.3 | 1.5 | I |
| My1-2-2-26 | 258 | 181 | 1.43 | 5.04 | 685 | 0.12105 | 0.00848 | 0.01863 | 0.00032 | 119.0 | 2.0 | I |
| MY1211-1.1 | 138 | 133 | 1.04 | / | / | 0.16380 | 0.00056 | 0.02021 | 0.00018 | 129.0 | 2.3 | II |
| MY1211-1.2 | 221 | 198 | 1.11 | / | / | 0.12200 | 0.0019 | 0.01896 | 0.00019 | 121.1 | 2.3 | II |
| MY1211-1.3 | 200 | 182 | 1.10 | / | / | 0.15200 | 0.0016 | 0.0202 | 0.00019 | 128.9 | 2.5 | II |
| MY1211-1.4 | 133 | 151 | 0.88 | / | / | 0.12600 | 0.0018 | 0.01851 | 0.00028 | 118.2 | 3.3 | II |
| MY1211-1.5 | 337 | 231 | 1.46 | / | / | 0.12000 | 0.0015 | 0.01944 | 0.00018 | 124.1 | 2.3 | II |
| MY1211-1.6 | 152 | 153 | 0.99 | / | / | 0.09800 | 0.003 | 0.01875 | 0.00036 | 119.8 | 4.3 | II |
| MY1211-1.7 | 427 | 275 | 1.55 | / | / | 0.10300 | 0.0018 | 0.01863 | 0.00021 | 119.0 | 2.5 | II |
| MY1211-1.8 | 169 | 150 | 1.13 | / | / | 0.12900 | 0.0029 | 0.01905 | 0.00025 | 121.6 | 3.0 | II |
| MY1211-1.9 | 247 | 210 | 1.18 | / | / | 0.13100 | 0.0011 | 0.01931 | 0.00019 | 123.3 | 2.3 | II |
| MY1211-1.10 | 172 | 162 | 1.06 | / | / | 0.10500 | 0.0031 | 0.01928 | 0.00029 | 123.1 | 3.5 | II |
| MY1211-1.11 | 258 | 211 | 1.23 | / | / | 0.07900 | 0.0018 | 0.01884 | 0.00017 | 120.3 | 2.1 | II |
| MY1211-1.12 | 402 | 238 | 1.69 | / | / | 0.13400 | 0.0015 | 0.0201 | 0.00018 | 128.3 | 2.3 | II |
| MY1211-1.13 | 219 | 189 | 1.16 | / | / | 0.15200 | 0.0013 | 0.02019 | 0.00019 | 128.9 | 2.4 | II |
| MY1211-1.14 | 139 | 155 | 0.90 | / | / | 0.11900 | 0.0018 | 0.01918 | 0.0002 | 122.5 | 2.4 | II |
| MY1211-1.15 | 228 | 170 | 1.34 | / | / | 0.08700 | 0.0032 | 0.01915 | 0.00029 | 122.3 | 3.5 | II |
| MY1211-1.16 | 136 | 152 | 0.90 | / | / | 0.14400 | 0.0027 | 0.01966 | 0.00026 | 125.5 | 3.3 | II |
| MY1211-1.17 | 420 | 271 | 1.55 | / | / | 0.11000 | 0.0021 | 0.01823 | 0.00023 | 116.4 | 2.6 | II |

Notes: common Pb corrections are from Andersen [36]. I: method for LA-ICP-MS; II: method for the SHRIMP II technique. “/” for null for SHRIMP II method.

Despite uncertainty, two analytical methods were consistent, and both indicated that the Caochang monzonitic granitic pluton was crystallized at the Aptian stage of the Early Cretaceous, corresponding to the volcanic activities of the Qingshan Group in the study area [11].

4.2. Zircon Hf–O Isotopic Results.

A total of 40 in situ zircon Lu–Hf analyses were conducted on samples of My121 and My122 (one spot was excluded). The analytical data of zircon Lu–Hf are shown in Table 2. The analytical results revealed that values of ¹⁷⁶Lu/¹⁷⁷Hf ranged from 0.000621 to 0.00314 (mean value = 0.001215), with the majority of Lu–Hf spots having a low value (low accumulation) (<0.002), corresponding to a high

quality of data (Figure 5a). The $\epsilon_{\text{Hf}}(t)$ values of assayed zircons ranged from -27.51 to -32.35 , with a mean value of -30.21 (Figure 5b,c), and two-stage model ages (T_{DM2}) varied from 2979 to 3175 Ma, with a mean age of 3053 Ma (Figure 5d).

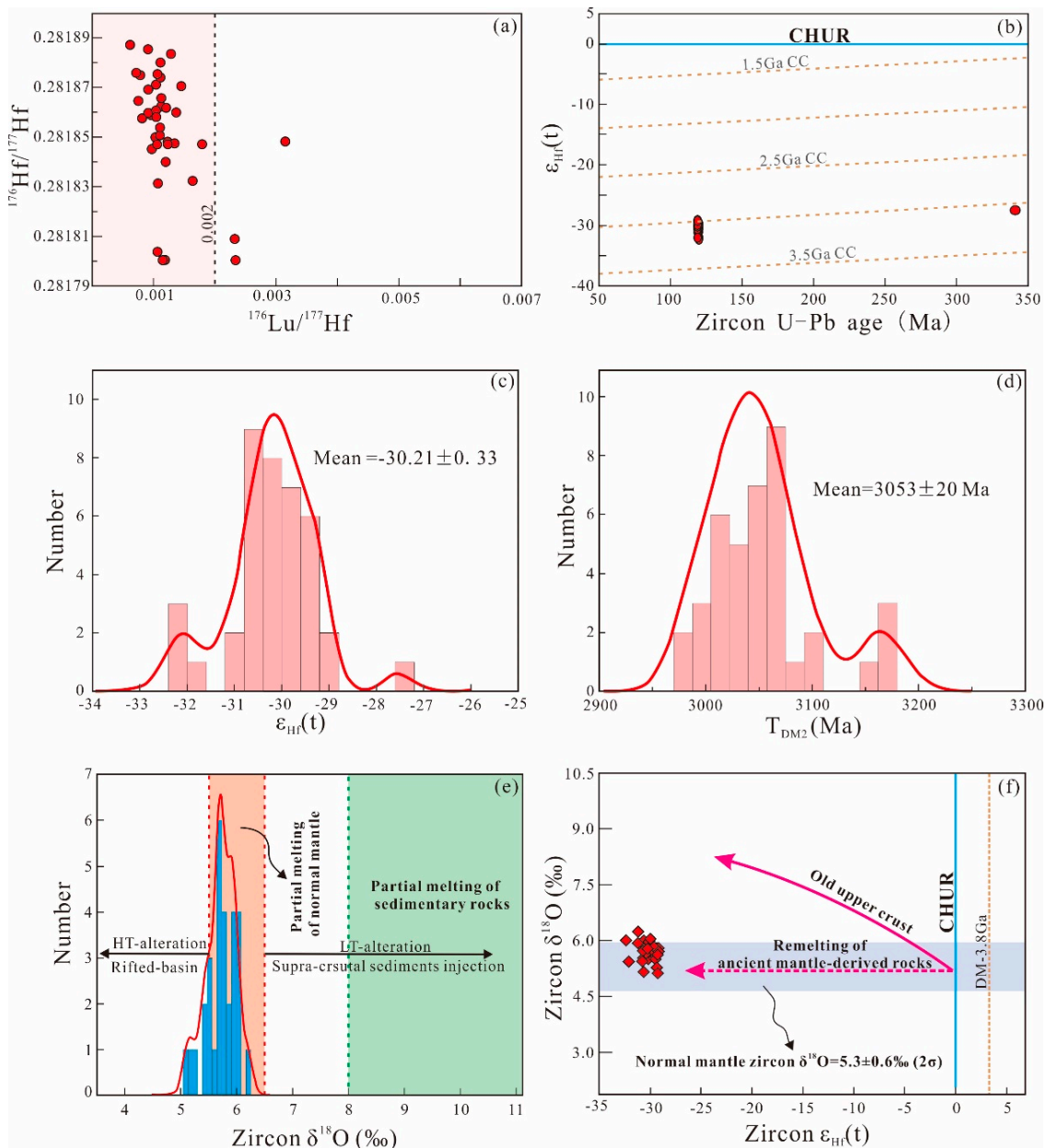


Figure 5. Zircon Hf-O isotopic results. (a) $^{176}\text{Lu}/^{177}\text{Hf}$ versus $^{176}\text{Hf}/^{177}\text{Hf}$ diagram. (b) Zircon U-Pb age versus $\epsilon_{\text{Hf}}(t)$ diagram. (c) Histogram of $\epsilon_{\text{Hf}}(t)$ values. (d) Histogram of the two-stage model age (T_{DM2}). (e) Histogram of zircon oxygen isotopes. (f) Zircon $\delta^{18}\text{O}$ values versus $\epsilon_{\text{Hf}}(t)$ values. CC: continental crust; CHUR: chondritic uniform reservoir; red dot for zircon Hf isotopic value, one red dot representing one datum; red diamond for zircon oxygen value, one diamond for one oxygen datum

Table 2. Zircon Lu–Hf isotopic results of the granitic pluton in the study area.

| Spot Number | Age | $^{176}\text{Hf}/^{177}\text{Hf}$ | 1 σ | $^{176}\text{Lu}/^{177}\text{Hf}$ | 1 σ | $^{176}\text{Yb}/^{177}\text{Hf}$ | 1 σ | I_{Hf} | $\epsilon_{\text{Hf}}(t)$ | 1 σ | $f_{\text{Lu/Hf}}$ | T_{DM1} | 1 σ | T_{DM2} | 1 σ |
|-------------|-----|-----------------------------------|------------|-----------------------------------|------------|-----------------------------------|------------|-----------------|---------------------------|------------|--------------------|------------------|------------|------------------|------------|
| My121-01 | 120 | 0.281840 | 0.000009 | 0.001198 | 0.000007 | 0.027346 | 0.000178 | 0.28184 | −30.43 | 0.32 | −0.96 | 1992 | 12 | 3084 | 19 |
| My121-02 | 120 | 0.281804 | 0.000009 | 0.001066 | 0.000004 | 0.024296 | 0.000079 | 0.28180 | −32.13 | 0.31 | −0.97 | 2036 | 12 | 3163 | 19 |
| My121-04 | 120 | 0.281848 | 0.000008 | 0.001230 | 0.000005 | 0.028240 | 0.000122 | 0.28185 | −30.57 | 0.30 | −0.96 | 1983 | 12 | 3066 | 18 |
| My121-05 | 120 | 0.281869 | 0.000009 | 0.000914 | 0.000014 | 0.021804 | 0.000406 | 0.28187 | −29.80 | 0.32 | −0.97 | 1938 | 13 | 3019 | 20 |
| My121-06 | 341 | 0.281801 | 0.000008 | 0.001190 | 0.000039 | 0.031458 | 0.001135 | 0.28179 | −27.51 | 0.30 | −0.96 | 2047 | 12 | 3042 | 18 |
| My121-08 | 120 | 0.281859 | 0.000009 | 0.000965 | 0.000006 | 0.021987 | 0.000117 | 0.28186 | −29.74 | 0.33 | −0.97 | 1954 | 13 | 3042 | 20 |
| My121-09 | 120 | 0.281875 | 0.000009 | 0.000785 | 0.000008 | 0.018712 | 0.000174 | 0.28187 | −29.59 | 0.33 | −0.98 | 1923 | 13 | 3006 | 20 |
| My121-10 | 120 | 0.281845 | 0.000009 | 0.000973 | 0.000013 | 0.022548 | 0.000282 | 0.28184 | −30.66 | 0.32 | −0.97 | 1974 | 12 | 3072 | 20 |
| My121-11 | 120 | 0.281847 | 0.000009 | 0.001342 | 0.000012 | 0.032351 | 0.000303 | 0.28184 | −30.60 | 0.33 | −0.96 | 1990 | 13 | 3068 | 20 |
| My121-12 | 120 | 0.281860 | 0.000010 | 0.001369 | 0.000007 | 0.032400 | 0.000172 | 0.28186 | −30.16 | 0.37 | −0.96 | 1974 | 15 | 3041 | 23 |
| My121-13 | 120 | 0.281800 | 0.000010 | 0.001151 | 0.000005 | 0.026790 | 0.000123 | 0.28180 | −31.82 | 0.35 | −0.97 | 2045 | 14 | 3171 | 22 |
| My121-14 | 120 | 0.281831 | 0.000009 | 0.001071 | 0.000001 | 0.024793 | 0.000044 | 0.28183 | −31.15 | 0.32 | −0.97 | 1998 | 12 | 3103 | 19 |
| My121-15 | 120 | 0.281850 | 0.000008 | 0.001030 | 0.000006 | 0.024307 | 0.000174 | 0.28185 | −30.49 | 0.29 | −0.97 | 1970 | 11 | 3062 | 18 |
| My121-16 | 120 | 0.281800 | 0.000011 | 0.002338 | 0.000043 | 0.056820 | 0.001104 | 0.28180 | −32.35 | 0.38 | −0.93 | 2111 | 15 | 3175 | 23 |
| My121-17 | 120 | 0.281847 | 0.000010 | 0.001233 | 0.000020 | 0.028555 | 0.000421 | 0.28184 | −30.61 | 0.37 | −0.96 | 1984 | 15 | 3069 | 23 |
| My121-18 | 120 | 0.281858 | 0.000009 | 0.000813 | 0.000002 | 0.019332 | 0.000029 | 0.28186 | −29.78 | 0.31 | −0.98 | 1948 | 12 | 3044 | 19 |
| My121-19 | 120 | 0.281862 | 0.000009 | 0.001128 | 0.000006 | 0.027226 | 0.000113 | 0.28186 | −30.06 | 0.31 | −0.97 | 1958 | 12 | 3035 | 19 |
| My122-01 | 119 | 0.281832 | 0.000009 | 0.001638 | 0.000021 | 0.039715 | 0.000564 | 0.28183 | −31.18 | 0.33 | −0.95 | 2027 | 13 | 3103 | 20 |
| My122-02 | 119 | 0.281860 | 0.000010 | 0.000915 | 0.000004 | 0.021709 | 0.000130 | 0.28186 | −30.16 | 0.35 | −0.97 | 1951 | 14 | 3040 | 21 |
| My122-03 | 119 | 0.281851 | 0.000009 | 0.001102 | 0.000009 | 0.025715 | 0.000200 | 0.28185 | −30.49 | 0.32 | −0.97 | 1973 | 13 | 3061 | 20 |
| My122-04 | 119 | 0.281847 | 0.000008 | 0.001058 | 0.000006 | 0.025040 | 0.000122 | 0.28184 | −30.19 | 0.29 | −0.97 | 1975 | 12 | 3069 | 18 |
| My122-05 | 119 | 0.281854 | 0.000009 | 0.001105 | 0.000018 | 0.026502 | 0.000496 | 0.28185 | −30.38 | 0.32 | −0.97 | 1968 | 13 | 3054 | 20 |
| My122-06 | 119 | 0.281884 | 0.000008 | 0.001285 | 0.000006 | 0.030369 | 0.000140 | 0.28188 | −29.34 | 0.29 | −0.96 | 1937 | 11 | 2989 | 18 |
| My122-07 | 119 | 0.281848 | 0.000010 | 0.003147 | 0.000051 | 0.078701 | 0.001352 | 0.28184 | −30.74 | 0.37 | −0.91 | 2088 | 16 | 3074 | 23 |
| My122-08 | 119 | 0.281880 | 0.000011 | 0.001113 | 0.000067 | 0.026345 | 0.001534 | 0.28188 | −29.46 | 0.38 | −0.97 | 1933 | 15 | 2997 | 23 |
| My122-09 | 119 | 0.281871 | 0.000009 | 0.001041 | 0.000015 | 0.024160 | 0.000300 | 0.28187 | −29.34 | 0.31 | −0.97 | 1941 | 12 | 3016 | 19 |
| My122-10 | 119 | 0.281865 | 0.000008 | 0.000753 | 0.000009 | 0.017240 | 0.000179 | 0.28186 | −29.97 | 0.30 | −0.98 | 1936 | 12 | 3029 | 18 |
| My122-11 | 119 | 0.281862 | 0.000009 | 0.001206 | 0.000021 | 0.028586 | 0.000564 | 0.28186 | −30.11 | 0.32 | −0.96 | 1963 | 13 | 3037 | 20 |
| My122-12 | 119 | 0.281871 | 0.000009 | 0.001453 | 0.000071 | 0.037634 | 0.001977 | 0.28187 | −29.82 | 0.34 | −0.96 | 1963 | 14 | 3019 | 21 |
| My122-13 | 119 | 0.281861 | 0.000008 | 0.001040 | 0.000005 | 0.024390 | 0.000134 | 0.28186 | −30.13 | 0.29 | −0.97 | 1956 | 12 | 3039 | 18 |
| My122-15 | 119 | 0.281874 | 0.000009 | 0.001114 | 0.000004 | 0.026054 | 0.000099 | 0.28187 | −29.24 | 0.30 | −0.97 | 1941 | 12 | 3010 | 19 |
| My122-16 | 119 | 0.281887 | 0.000009 | 0.000621 | 0.000024 | 0.014994 | 0.000592 | 0.28189 | −29.16 | 0.30 | −0.98 | 1898 | 12 | 2979 | 18 |
| My122-18 | 119 | 0.281875 | 0.000008 | 0.001066 | 0.000013 | 0.024323 | 0.000330 | 0.28187 | −29.62 | 0.29 | −0.97 | 1937 | 11 | 3007 | 18 |
| My122-19 | 119 | 0.281847 | 0.000012 | 0.001792 | 0.000014 | 0.043603 | 0.000350 | 0.28184 | −30.67 | 0.43 | −0.95 | 2014 | 17 | 3071 | 27 |
| My122-20 | 119 | 0.281858 | 0.000009 | 0.001045 | 0.000006 | 0.024099 | 0.000134 | 0.28186 | −30.23 | 0.31 | −0.97 | 1960 | 12 | 3044 | 19 |
| My122-21 | 119 | 0.281876 | 0.000009 | 0.000720 | 0.000007 | 0.016596 | 0.000204 | 0.28187 | −29.14 | 0.32 | −0.98 | 1919 | 12 | 3004 | 20 |
| My122-22 | 119 | 0.281866 | 0.000008 | 0.001126 | 0.000014 | 0.026669 | 0.000330 | 0.28186 | −29.96 | 0.27 | −0.97 | 1953 | 11 | 3028 | 17 |
| My122-23 | 119 | 0.281809 | 0.000010 | 0.002324 | 0.000056 | 0.057767 | 0.001431 | 0.28180 | −32.06 | 0.37 | −0.93 | 2098 | 15 | 3157 | 23 |
| My122-26 | 119 | 0.281885 | 0.000009 | 0.000911 | 0.000012 | 0.020823 | 0.000306 | 0.28188 | −29.25 | 0.31 | −0.97 | 1915 | 12 | 2984 | 19 |

Thirty representative zircon grains were selected for in situ oxygen analyses. The oxygen isotopic results are listed in Table 3. Analytical results revealed that zircon grains had a narrow range of $\delta^{18}\text{O}$ values (5.12–6.24‰) that were consistent with the normal mantle range (Figure 5e), reflecting partial melting of normal mantle material or rocks. The decoupling of Hf–O isotopes suggests that the granitic pluton originated from an ancient mafic lower crust-dominated source (Figure 5f).

Table 3. Zircon oxygen isotopic results of the granitic pluton in the study area.

| Sample Number | Zircon $\delta^{18}\text{O}$ (‰) | 2σ |
|---------------|----------------------------------|-----------|
| MY1211-1 | 5.53 | 0.20 |
| MY1211-10 | 6.00 | 0.21 |
| MY1211-11 | 5.50 | 0.16 |
| MY1211-12 | 6.24 | 0.17 |
| MY1211-13 | 5.85 | 0.15 |
| MY1211-14 | 6.01 | 0.24 |
| MY1211-15 | 5.16 | 0.26 |
| MY1211-16 | 5.68 | 0.20 |
| MY1211-17 | 5.99 | 0.18 |
| MY1211-18 | 5.93 | 0.16 |
| MY1211-19 | 5.68 | 0.14 |
| MY1211-2 | 5.68 | 0.18 |
| MY1211-20 | 5.66 | 0.14 |
| MY1211-21 | 5.79 | 0.24 |
| MY1211-22 | 5.44 | 0.18 |
| MY1211-23 | 5.50 | 0.29 |
| MY1211-24 | 5.27 | 0.21 |
| MY1211-25 | 5.92 | 0.16 |
| MY1211-26 | 5.94 | 0.20 |
| MY1211-27 | 5.76 | 0.14 |
| MY1211-28 | 5.97 | 0.21 |
| MY1211-29 | 5.12 | 0.18 |
| MY1211-3 | 5.79 | 0.20 |
| MY1211-30 | 5.83 | 0.23 |
| MY1211-4 | 5.72 | 0.12 |
| MY1211-5 | 5.78 | 0.22 |
| MY1211-6 | 5.70 | 0.16 |
| MY1211-7 | 6.04 | 0.20 |
| MY1211-8 | 5.43 | 0.18 |
| MY1211-9 | 5.62 | 0.23 |

4.3. Whole-Rock Geochemical Results

A total of nine representative samples were selected for whole-rock geochemical analyses. The analytical results are listed in Table 4. In the following diagrams, the major elements were recalculated to 100% on a volatile-free basis.

Table 4. Whole-rock geochemical results of the granitic pluton in the study area.

| Sample Number | My1-2-1 | My1-2-2 | My1-2-3 | My1-2-4 | My1-2-4-1 | My1-2-5 | My1-2-6 | My1-2-7 | My1-2-8 |
|---|---------|---------|---------|---------|-----------|---------|---------|---------|---------|
| SiO ₂ | 64.37 | 65.43 | 65.13 | 64.95 | 64.22 | 60.63 | 65.46 | 65.45 | 58.80 |
| TiO ₂ | 0.57 | 0.53 | 0.52 | 0.55 | 0.54 | 0.61 | 0.55 | 0.55 | 0.55 |
| Al ₂ O ₃ | 15.52 | 15.70 | 15.58 | 16.02 | 15.75 | 16.03 | 15.76 | 15.66 | 16.51 |
| ^T Fe ₂ O ₃ | 4.48 | 3.97 | 4.12 | 4.21 | 4.16 | 5.07 | 4.20 | 4.25 | 4.59 |
| Na ₂ O | 3.63 | 3.67 | 3.74 | 3.79 | 3.78 | 3.98 | 3.87 | 3.60 | 6.80 |
| K ₂ O | 3.56 | 3.25 | 3.65 | 3.31 | 3.64 | 3.29 | 3.37 | 3.58 | 1.49 |
| MgO | 2.11 | 1.76 | 1.76 | 2.00 | 1.81 | 2.60 | 2.02 | 2.02 | 1.66 |
| CaO | 3.39 | 3.31 | 2.81 | 3.73 | 2.98 | 3.73 | 3.27 | 3.52 | 4.47 |
| MnO | 0.11 | 0.12 | 0.15 | 0.07 | 0.14 | 0.18 | 0.12 | 0.07 | 0.17 |
| P ₂ O ₅ | 0.21 | 0.19 | 0.19 | 0.20 | 0.21 | 0.23 | 0.21 | 0.21 | 0.20 |
| LOI | 1.62 | 2.16 | 2.75 | 0.57 | 2.6 | 3.47 | 1.51 | 0.89 | 4.51 |
| Total | 99.57 | 100.09 | 100.40 | 99.40 | 99.83 | 99.82 | 100.34 | 99.80 | 99.75 |
| Al | 83884 | 84875 | 84467 | 85816 | 85758 | 88080 | 84423 | 83818 | 91774 |
| Li | 13.00 | 15.80 | 19.50 | 10.40 | 15.70 | 25.70 | 16.90 | 10.20 | 5.07 |
| Be | 1.60 | 2.09 | 2.75 | 1.54 | 2.43 | 2.66 | 1.82 | 1.44 | 2.91 |
| Sc | 16.80 | 14.10 | 15.60 | 14.20 | 17.90 | 20.60 | 16.60 | 17.30 | 13.50 |
| Ti | 3547 | 3195 | 3207 | 3408 | 3378 | 3792 | 3406 | 3430 | 3504 |
| V | 74.70 | 67.10 | 67.80 | 69.20 | 67.70 | 87.30 | 72.40 | 70.60 | 61.50 |
| Cr | 24.10 | 20.80 | 20.40 | 23.30 | 20.80 | 60.80 | 23.00 | 21.70 | 19.60 |
| Mn | 921 | 972 | 1194 | 598 | 1082 | 1423 | 967 | 613 | 1291 |
| Co | 11.70 | 10.40 | 10.50 | 11.30 | 10.80 | 14.40 | 11.00 | 11.20 | 11.20 |
| Ni | 13.50 | 11.70 | 12.10 | 13.10 | 12.70 | 27.20 | 13.30 | 12.70 | 13.00 |
| Cu | 8.20 | 6.96 | 6.87 | 9.23 | 6.95 | 9.62 | 6.64 | 9.41 | 4.66 |
| Zn | 56.20 | 52.90 | 79.40 | 51.80 | 67.10 | 72.60 | 64.10 | 50.70 | 67.60 |
| Ga | 17.90 | 17.20 | 18.00 | 18.40 | 18.00 | 19.20 | 18.20 | 18.10 | 19.90 |
| Rb | 77.90 | 64.20 | 97.50 | 62.50 | 81.10 | 78.20 | 76.60 | 67.00 | 47.20 |
| Sr | 547 | 469 | 423 | 580 | 495 | 518 | 581 | 565 | 317 |
| Y | 16.50 | 14.20 | 15.00 | 15.10 | 14.60 | 18.00 | 15.30 | 15.70 | 13.20 |
| Zr | 205 | 201 | 197 | 198 | 195 | 197 | 198 | 208 | 202 |
| Nb | 10.10 | 9.84 | 9.74 | 9.41 | 9.24 | 11.70 | 8.85 | 9.61 | 10.40 |
| Mo | 0.52 | 0.70 | 1.86 | 0.35 | 0.44 | 1.05 | 1.11 | 0.41 | 0.26 |
| Cd | <0.030 | 0.03 | 0.14 | <0.030 | <0.030 | <0.030 | 0.04 | 0.03 | <0.030 |
| Sn | 1.18 | 1.08 | 1.22 | 1.13 | 1.34 | 1.48 | 1.27 | 1.13 | 6.03 |

Table 4. Cont.

| Sample Number | My1-2-1 | My1-2-2 | My1-2-3 | My1-2-4 | My1-2-4-1 | My1-2-5 | My1-2-6 | My1-2-7 | My1-2-8 |
|-----------------------|---------|---------|---------|---------|-----------|---------|---------|---------|---------|
| Cs | 1.37 | 1.53 | 2.29 | 0.98 | 1.24 | 1.45 | 1.19 | 1.05 | 0.70 |
| Ba | 1741 | 1518 | 1395 | 1540 | 1736 | 1944 | 1583 | 1614 | 640 |
| Hf | 5.08 | 5.10 | 4.94 | 4.76 | 4.66 | 5.00 | 4.77 | 5.13 | 4.91 |
| Ta | 0.74 | 0.72 | 0.72 | 0.67 | 0.65 | 0.75 | 0.64 | 0.71 | 0.77 |
| W | 0.22 | 0.30 | 0.77 | 0.17 | 0.77 | 0.40 | 0.27 | 0.15 | 0.87 |
| Tl | 0.44 | 0.38 | 0.61 | 0.45 | 0.62 | 0.48 | 0.47 | 0.36 | 0.28 |
| Pb | 26.90 | 27.00 | 50.00 | 22.60 | 26.00 | 32.50 | 26.30 | 23.10 | 13.10 |
| Bi | 0.10 | 0.12 | 0.13 | 0.04 | 0.20 | 0.13 | 0.07 | 0.04 | 0.51 |
| Th | 8.58 | 10.00 | 11.70 | 10.10 | 8.08 | 8.62 | 9.18 | 9.65 | 8.67 |
| U | 1.83 | 1.86 | 2.03 | 2.14 | 1.92 | 3.07 | 1.59 | 2.01 | 3.38 |
| La | 38.40 | 36.40 | 48.70 | 44.30 | 42.70 | 40.00 | 48.30 | 49.70 | 42.40 |
| Ce | 69.20 | 56.90 | 79.40 | 73.90 | 69.60 | 69.40 | 78.10 | 79.90 | 72.30 |
| Pr | 8.24 | 7.33 | 8.60 | 8.36 | 8.24 | 8.48 | 8.72 | 9.10 | 7.90 |
| Nd | 29.70 | 25.50 | 29.00 | 28.90 | 28.30 | 30.40 | 29.40 | 31.00 | 26.80 |
| Sm | 4.74 | 4.11 | 4.35 | 4.47 | 4.47 | 5.04 | 4.47 | 4.69 | 4.12 |
| Eu | 1.21 | 1.09 | 1.09 | 1.14 | 1.19 | 1.23 | 1.17 | 1.18 | 0.99 |
| Gd | 4.74 | 3.99 | 4.43 | 4.54 | 4.36 | 4.88 | 4.55 | 4.61 | 4.01 |
| Tb | 0.60 | 0.52 | 0.54 | 0.55 | 0.54 | 0.62 | 0.55 | 0.58 | 0.50 |
| Dy | 3.02 | 2.58 | 2.72 | 2.72 | 2.63 | 3.14 | 2.71 | 2.85 | 2.39 |
| Ho | 0.65 | 0.54 | 0.58 | 0.57 | 0.54 | 0.67 | 0.57 | 0.58 | 0.49 |
| Er | 1.71 | 1.55 | 1.64 | 1.59 | 1.54 | 1.90 | 1.66 | 1.68 | 1.41 |
| Tm | 0.28 | 0.25 | 1.06 | 0.25 | 0.24 | 0.30 | 0.25 | 0.26 | 0.22 |
| Yb | 1.75 | 1.57 | 1.60 | 1.57 | 1.52 | 1.88 | 1.59 | 1.64 | 1.34 |
| Lu | 0.29 | 0.26 | 0.27 | 0.26 | 0.25 | 0.31 | 0.26 | 0.27 | 0.23 |
| 10000Ga/Al | 2.13 | 2.03 | 2.13 | 2.14 | 2.10 | 2.18 | 2.16 | 2.16 | 2.17 |
| FeO ^T /MgO | 1.91 | 2.03 | 2.11 | 1.89 | 2.07 | 1.76 | 1.87 | 1.89 | 2.49 |
| Zr+Nb+Ce+Y | 300.8 | 281.9 | 301.1 | 296.4 | 288.4 | 296.1 | 300.3 | 313.2 | 297.9 |
| A/CNK | 0.97 | 1.01 | 1.02 | 0.96 | 1.01 | 0.95 | 0.99 | 0.97 | 0.79 |
| A/NK | 1.58 | 1.64 | 1.54 | 1.63 | 1.55 | 1.58 | 1.57 | 1.60 | 1.29 |
| Nb/Th | 1.18 | 0.98 | 0.83 | 0.93 | 1.14 | 1.36 | 0.96 | 1.00 | 1.20 |
| (La/Yb) _N | 14.79 | 15.63 | 20.52 | 19.02 | 18.94 | 14.34 | 20.48 | 20.43 | 21.33 |
| Mg [#] | 49 | 47 | 46 | 49 | 47 | 51 | 49 | 49 | 42 |

Table 4. Cont.

| Sample Number | My1-2-1 | My1-2-2 | My1-2-3 | My1-2-4 | My1-2-4-1 | My1-2-5 | My1-2-6 | My1-2-7 | My1-2-8 |
|---|---------|---------|---------|---------|-----------|---------|---------|---------|---------|
| (K ₂ O+Na ₂ O)/CaO | 2.12 | 2.09 | 2.63 | 1.90 | 2.49 | 1.95 | 2.21 | 2.04 | 1.85 |
| K ₂ O+Na ₂ O | 7.19 | 6.92 | 7.39 | 7.10 | 7.42 | 7.27 | 7.24 | 7.18 | 8.29 |
| Sr/CaO | 161 | 142 | 151 | 155 | 166 | 139 | 178 | 161 | 71 |
| (Dy/Yb) _N | 1.12 | 1.07 | 1.10 | 1.12 | 1.12 | 1.08 | 1.11 | 1.13 | 1.16 |
| Zr/Hf | 40.35 | 39.41 | 39.88 | 41.60 | 41.85 | 39.40 | 41.51 | 40.55 | 41.14 |
| Rb/Sr | 0.14 | 0.14 | 0.23 | 0.11 | 0.16 | 0.15 | 0.13 | 0.12 | 0.15 |
| Sr/Y | 33.15 | 33.03 | 28.20 | 38.41 | 33.90 | 28.78 | 37.97 | 35.99 | 24.02 |
| SiO ₂ /Al ₂ O ₃ | 4.15 | 4.17 | 4.18 | 4.05 | 4.08 | 3.78 | 4.15 | 4.18 | 3.56 |
| Al ₂ O ₃ /MgO | 7.36 | 8.92 | 8.85 | 8.01 | 8.70 | 6.17 | 7.80 | 7.75 | 9.95 |
| CaO/Al ₂ O ₃ | 0.22 | 0.21 | 0.18 | 0.23 | 0.19 | 0.23 | 0.21 | 0.22 | 0.27 |
| A.R. | 1.38 | 1.33 | 1.40 | 1.33 | 1.39 | 1.32 | 1.35 | 1.37 | 1.11 |
| Al ₂ O ₃ /(MgO+FeO ^T) | 1.40 | 1.64 | 1.60 | 1.53 | 1.59 | 1.22 | 1.50 | 1.48 | 1.64 |
| CaO/(MgO+FeO ^T) | 0.56 | 0.63 | 0.53 | 0.65 | 0.55 | 0.52 | 0.57 | 0.61 | 0.81 |
| Molar (N+K)/(F+M+T) | 0.83 | 0.94 | 0.97 | 0.88 | 0.96 | 0.73 | 0.89 | 0.87 | 1.19 |
| N+K+F+M+T | 14.19 | 13.05 | 13.70 | 13.60 | 13.90 | 15.61 | 13.75 | 13.72 | 15.36 |
| Yb _N | 8.37 | 7.51 | 7.66 | 7.51 | 7.27 | 9.00 | 7.61 | 7.85 | 6.41 |
| LREE/HREE | 11.62 | 11.66 | 13.33 | 13.37 | 13.30 | 11.28 | 14.02 | 14.08 | 14.59 |
| ∑REE | 164.53 | 142.59 | 183.98 | 173.12 | 166.12 | 168.25 | 182.30 | 188.04 | 165.10 |
| LREE | 156.23 | 135.32 | 175.57 | 165.61 | 158.86 | 159.43 | 174.71 | 180.18 | 158.52 |
| Eu/Eu* | 0.78 | 0.82 | 0.76 | 0.77 | 0.82 | 0.76 | 0.79 | 0.78 | 0.74 |
| CIPW calculated results (%) | | | | | | | | | |
| Ab | 31.00 | 31.16 | 31.66 | 32.41 | 32.19 | 33.92 | 32.79 | 30.67 | 57.96 |
| Or | 21.23 | 19.27 | 21.58 | 19.77 | 21.65 | 19.58 | 19.94 | 21.30 | 8.87 |
| An | 15.68 | 15.23 | 12.70 | 17.10 | 13.50 | 16.27 | 15.70 | 16.10 | 10.20 |
| Plagioclase An number | 32 | 32 | 27 | 33 | 28 | 31 | 31 | 33 | 14 |

Abbreviation notes. A.R. = (Al₂O₃ + CaO + Na₂O + K₂O)/(Al₂O₃ + CaO - Na₂O - K₂O); (N + K)/(F + M + T) = (Na₂O + K₂O)/(FeO^T + MgO + TiO₂); N + K + F + M + T = Na₂O + K₂O + FeO^T + MgO + TiO₂. ∑REE: total rare earth element; LREE: light REE; HREE: heavy REE; LOI: loss on ignition. Eu/Eu* representing Eu element anomaly; An: anorthite.

In the TAS diagram, the samples are plotted in the granodiorite to quartz monzonite fields (Figure 7a). According to the CIPW results and mineral features, we identified the identified pluton as monzonitic granite. The studied samples showed calc-alkaline features, as suggested by the A.R. versus SiO_2 diagram (Figure 7b). A further classification diagram suggested that the monzonitic granite belonged to high-K calc-alkaline series, but one sample fell in the medium-K calc-alkaline field that might be related to magma mixing (with greater MME composition participation) (Figure 7c). In the molar $\text{Al}_2\text{O}_3/\text{CaO} + \text{Na}_2\text{O} + \text{K}_2\text{O}$ (A/CNK) versus molar $\text{Al}_2\text{O}_3/\text{Na}_2\text{O} + \text{K}_2\text{O}$ (A/NK) diagram (Figure 7d), the studied samples demonstrated metaluminous affinity corresponding to I-type granite. Detailed petrogenetic classifications are discussed below.

The total rare earth element ($\sum\text{REE}$) contents ranged from 143 to 188 ppm, and light REE (LREE)/heavy REE (HREE) and $(\text{La}/\text{Yb})_N$ ratios varied from 11.28 to 14.59 and from 14.34 to 21.33, respectively, both suggesting an enrichment of LREE compared to HREE (Figure 6a). In addition, the samples showed weak Eu anomalies, with Eu/Eu^* ratios varying from 0.76 to 0.82 (mean ratio = 0.78). In the primitive-normalized spider diagram (Figure 6b), the majority of samples were enriched in large-ion lithophile elements (e.g., Cs, K, Ba, and LREE), but depleted in high-field-strength elements (HSFE), suggesting an arc-type or crustal magma nature [37]. Additionally, the samples were enriched in Pb, Zr, and Hf, also corresponding to crustal affinity. Combined with above geochemical features, we tentatively argue that the Caochang granitic pluton is most probably a result of the partial melting of crustal material; detailed petrogenetic process of the granitic pluton and deep insights are addressed below.

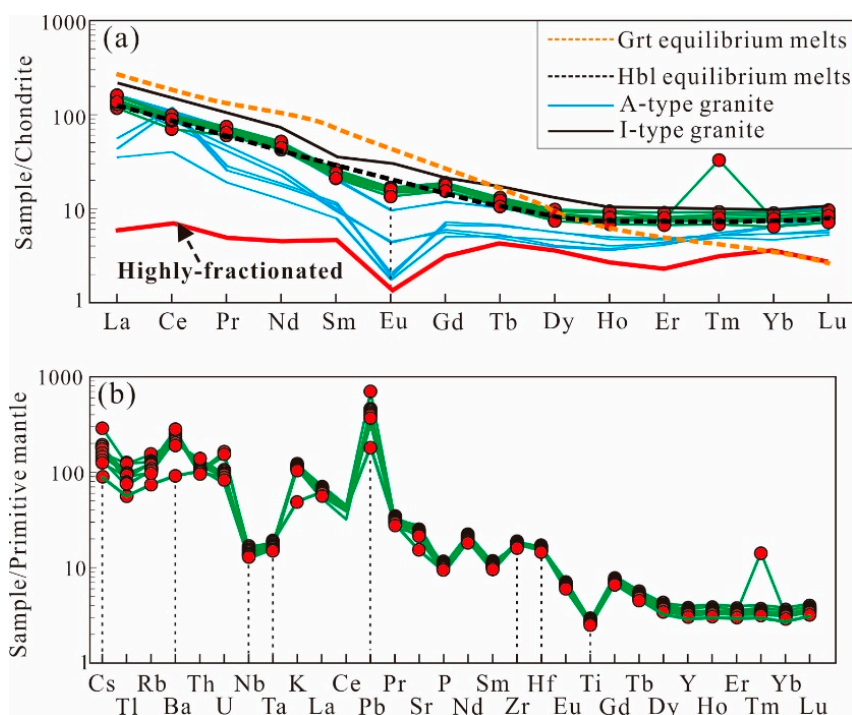


Figure 6. (a) Chondrite-normalized REE patterns (garnet and hornblende equilibrium melt modeling curves are from Moyen [43]; highly-fractionated magma curve are from Sun [44]) (red dot for the studied samples). (b) Primitive mantle-normalized multiple trace element diagram (chondrite normalization values are from Boynton [45]; primitive mantle normalization values are from Sun [46]).

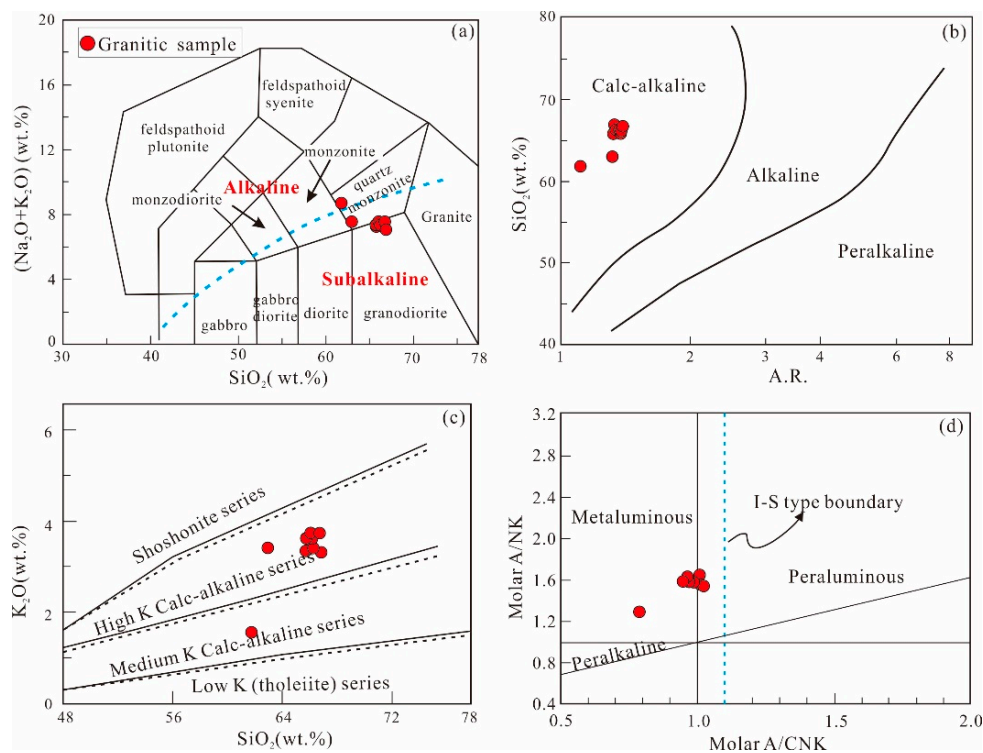


Figure 7. (a) TAS diagram (from Middlemost [38]) (red dot for the studied samples). The dotted line shows the Irvine line (from Irvine and Baragar [39]), while the area below the dotted line is sub-alkaline, and that above the dotted line is alkaline. (b) Alkalinity ratio (A.R.) versus SiO_2 plot (after Wright [40]). (c) SiO_2 versus K_2O plot (from Peccerillo [41]). (d) A/CNK versus A/NK plot (from Maniar and Piccoli [42]).

5. Discussion

5.1. Classification for the Granitic Pluton

According to petrogenetic setting and magma source, granitoids can be divided into the M-, I-, A-, and S-types [47]. A-type granites are usually produced in high-temperature anorogenic settings (e.g., the extensional setting), and are marked by high alkaline contents and anhydrous features [48,49]. It is well recognized that eastern China experienced strongly lithospheric thinning (foundering) during the Early Cretaceous (ca. 125 Ma) [50], leading to massive mantle magma underplating and extensional tectonic formation (e.g., the metamorphic core complex). Thus, the underplating of mantle magma with the heat flux and extensional tectonics provided an advantage for the formation of A-type granites in the study region during the Early Cretaceous. Considering this, we will evaluate the possibility that is akin to A-type granite in the study region.

Discrimination diagrams revealed that the studied samples belonged to ordinary granite, excluding the A-type possibility (Figure 8a–c). Additionally, the combination of whole-rock Zr and zircon Ti thermometers revealed a low crystallization temperature [51] (Figure 8d,e) that is inconsistent with typical high-temperature A-type granite [49]. The normalized-REE patterns were in agreement with I-type granitic rocks that were reported in the Sulu orogenic belt [20,52] (Figure 6a). Typical A-type granitic rocks, which were reported in the Sulu belt, showed significant a Eu-negative anomaly corresponding to highly-fractionated granite (Figure 6a) [20,23]. These genetic features suggest that the new identified granitic pluton belongs to I- or S-type granite rather than A-type and high-fractionated granite.

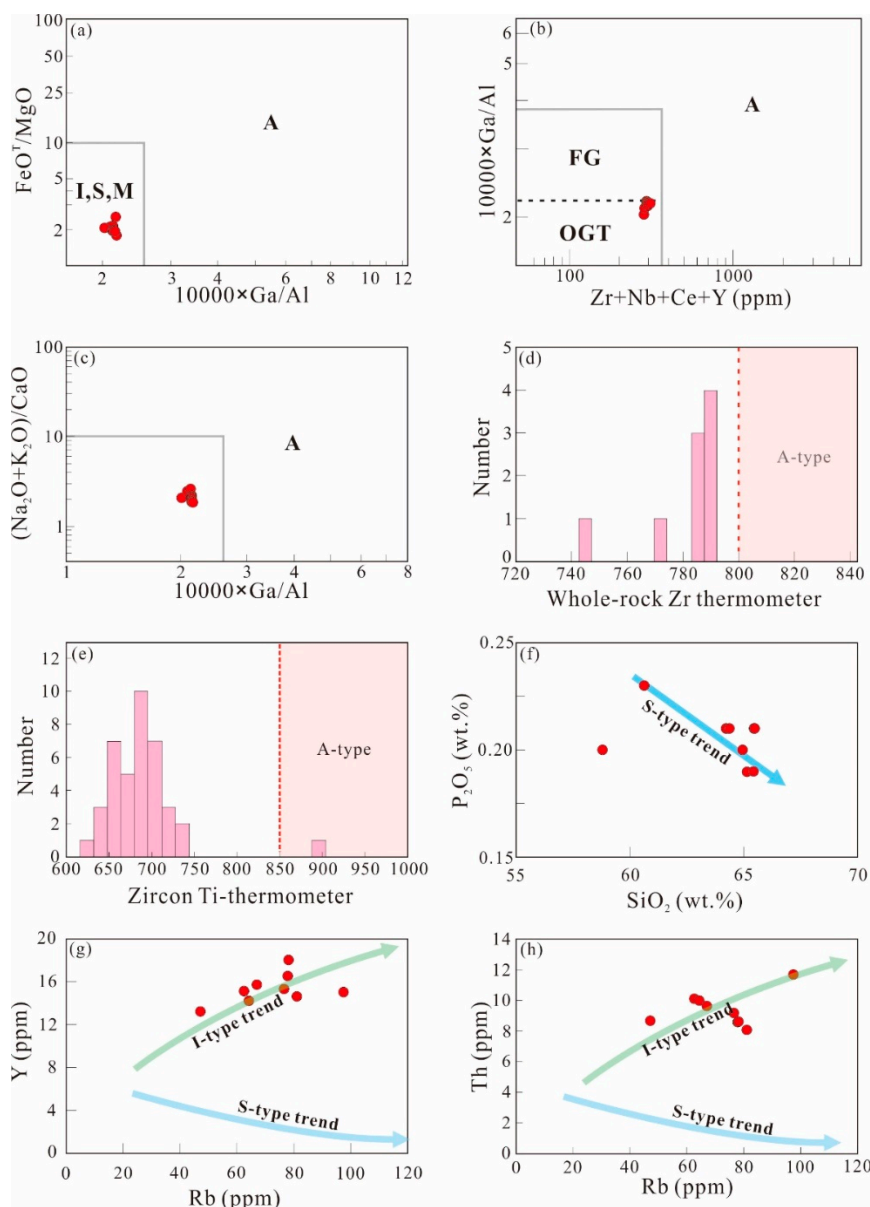


Figure 8. (a–c) Discrimination diagrams of A-type granite (from Whalen [53]) (red dot for the studied samples). (d,e) Whole-rock Zr and zircon Ti thermometers. (f) SiO_2 versus P_2O_5 diagram (from Chappell [54]). (g,h) Rb versus Y and Rb versus Th diagrams (from Chappell [55]).

Additionally, in the SiO_2 versus P_2O_5 diagram (Figure 8f), P_2O_5 shows a decreasing trend with increasing SiO_2 , corresponding to I-type granite [54]. In addition, Rb versus Y and Rb versus Th discriminate diagrams also suggest an I-type granitic trend for the studied samples in this study (Figure 8g,h). In addition, low zircon $\delta^{18}\text{O}$ values of 5.12–6.24‰ exclude the possibility of S-type granite (Figure 5e). It is well known that granites sourced from partial melting of sedimentary rocks or reworking of S-type granites will have high zircon $\delta^{18}\text{O}$ values (>8‰), indicating a supra-crustal interaction [56–58]. In addition, microstructural analyses revealed that the granitic samples correspond with I-type granite, comprising plagioclase, K-feldspar, quartz, and biotite (Figure 2c–e). Compared to I-type granite, S-type granite is rich in high-aluminum (Al) minerals (e.g., muscovite, cordierite, and garnet). In conclusion, the granitic pluton identified in the Caochang region is composed of typical I-type granite that originated from the partial melting of meta-igneous rocks.

5.2. Magma Source and Petrogenesis

Multiple studies have demonstrated that the granites are products of partial melting of the Yangtze crustal material, as suggested by low values of oxygen isotopes and Neoproterozoic (600–800 Ma) inherited zircons in the Sulu orogenic belt [4,5,11]. However, magmatic rocks collected from the North China craton (NCC) have high values of oxygen isotopes and Archean inherited zircons. The Wulian (Baichihe)–Qingdao–Yantai fault (WQYF) is regarded as the boundary of the Yangtze and the NCC. It is clear that granites collected from the west of the WQYF show a genetic association with partial melting of the NCC crustal material, whereas those from the east of the WQYF have a close relation with the Yangtze craton [4,27,28]. However, the nature of granites from the fault zone and neighboring regions (tectonic amalgamation region) is poorly understood. Recently, Zhao [59] provided a summary and proposed that the granites across the fault zone and neighboring regions all belong to the Yangtze craton. This statement implies that granites distributed in the Sulu belt and boundary region have a close affinity with the Yangtze craton. According to Zhao's [59] proposal, our samples, which are located in the east of the fault zone (Figure 1b), have a close affinity with the Yangtze craton. Additionally, the absence of the Archean inherited zircons also rules out the possibility of the NCC (Figure 4).

The zircon Lu–Hf isotope is a useful tool in discriminating magma sources and petrogenetic processes [60]. The analytical results revealed that the granitic samples have homogeneous Hf isotopic compositions, with narrow variations of $\epsilon_{\text{Hf}}(t)$ values ranging from -27.51 to -32.35 . In addition, most of the zircons have low values of $^{176}\text{Lu}/^{177}\text{Hf}$ (Figure 5a) (<0.002), suggesting a good quality of data [61]. It is well established that positive $\epsilon_{\text{Hf}}(t)$ values suggest a crustal growth or recycling of juvenile crust, and negative $\epsilon_{\text{Hf}}(t)$ values represent ancient crustal recycling or reworking. The newly identified granite showed strongly negative $\epsilon_{\text{Hf}}(t)$ values (-27.51 to -32.35 , mean value: -30.21) (Figure 5b,c), indicating that the magma source of the studied pluton was derived from partial melting of ancient crust. The two-stage Hf model ages ranged from 2979 to 3175 Ma (mean age: 3053 Ma) (Figure 5d), also indicating partial melting of the Mesoarchean crustal material. In conclusion, we argue that the granitic pluton is derived from partial melting of the Yangtze ancient crustal material. The strongly negative $\epsilon_{\text{Hf}}(t)$ values suggest multiple reworking of the magma source.

As described above, the granitic pluton originated from partial melting of the Yangtze crustal material. The effective geochemical diagrams indicate that the newly identified pluton was derived from partial melting of mafic material (Figure 9a,b). Compared to the middle-upper crust, the lower crust is mafic in composition [62,63]. Considering the previous argument, we argue that the granitic pluton originated due to the partial melting of the Yangtze mafic lower crust. Zhao [4] concluded that most of the Early Cretaceous granites occurring in the Sulu belt had normal oxygen ($\delta^{18}\text{O}$) values close to those of normal mantle zircons ($5.3 \pm 0.3\text{‰}$), suggesting a deep magma source with no significant water–rock interaction. If the rocks were derived from the middle-upper crust, they would experience significant influence of atmospheric precipitation, demonstrating low oxygen isotopes. In this study, our samples had $\delta^{18}\text{O}$ values of 5.12 – 6.25‰ that were consistent with juvenile basaltic crust (5.5 – 6.5‰) being formed by partial melting of mantle-derived magma [64] ($\delta = ^{18}\text{O}_{\text{Zrn}} = 5.3 \pm 0.3\text{‰}$) (Figure 5e), suggesting that the granite was probably derived from partial melting of basaltic lower crust and experienced negligible supra-crustal contamination in the parental magma. This was also indicated by coeval felsic volcanic rocks ($\delta^{18}\text{O} = 4.82$ – 5.86‰) on Lingshan Island [11].

Compared to zircon oxygen isotopic information, zircon Hf isotope is also a necessary requirement for constraining the formation and evolution of continental crust [60,65]. The combination of Hf–O isotopes is a very powerful tool for deciphering the nature of magma and the magmatic evolution process of host granites and mafic micro-granular enclaves [57,66]. Unlike the $\delta^{18}\text{O}$ results, the $\epsilon_{\text{Hf}}(t)$ values of the studied pluton displayed ancient crustal characteristics (Figure 5b, $\epsilon_{\text{Hf}}(t) = -27.51$ – -32.35). Furthermore, the zircon Hf two-stage model ages (T_{DM2}) showed Mesoarchean rocks from the Yangtze craton [67,68] (Figure 5d). Therefore, the studied zircons have mantle-derived oxygen isotopic information, whereas Hf isotopic compositions suggest ancient crustal features (Figure 5f). Under

most circumstances, significant negative $\varepsilon_{\text{Hf}}(t)$ values are associated with crustal material input, especially the supra-crustal sediments. In contrast, the zircon $\delta^{18}\text{O}$ isotopic values are very sensitive to supra-crustal material input. Crustal contamination will lead to sharp deviations from the mantle-like $\delta^{18}\text{O}$ values (Figure 5f). As a consequence, the correlation (Figure 5f) is not suitable via the assimilation fractional crystallization (AFC) process.

A tenable explanation for the correlation of $\delta^{18}\text{O}$ and $\varepsilon_{\text{Hf}}(t)$ values is that the Caochang granitic pluton potentially originated from partial melting of an ancient mafic lower crust. It has been demonstrated that a mafic lower crust derived from a depleted mantle can show enriched Hf isotopic compositions through a considerable period of time [60,69,70]. If supra-crustal materials were not injected and did not experience low- and high-temperature water–rock interactions, the mafic lower crust would have negligible variations of oxygen isotope values that retain the mantle-like $\delta^{18}\text{O}$ characteristics. Based on the above discussion, we propose that the Caochang granitic pluton derived from the partial melting of the mafic lower crust. This model is in agreement with the geochemical discrimination diagrams that suggest partial melting of the mafic lower crust (Figure 9a,b).

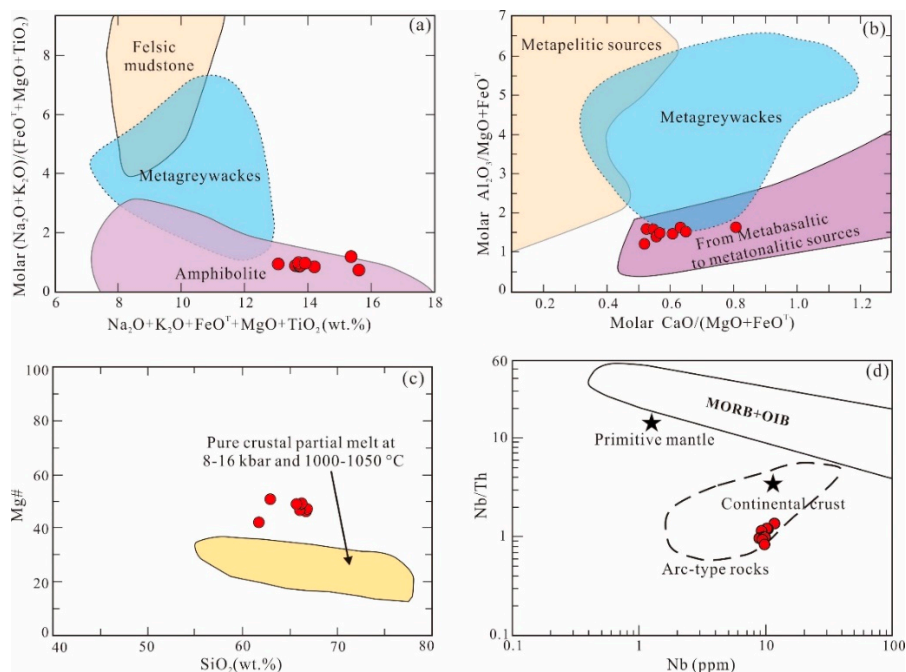


Figure 9. Compositional discrimination diagrams of granites (red dot for the studied samples). (a) $\text{Na}_2\text{O} + \text{K}_2\text{O} + \text{FeO} + \text{MgO} + \text{TiO}_2$ versus molar $(\text{Na}_2\text{O} + \text{K}_2\text{O})/(\text{FeO} + \text{MgO} + \text{TiO}_2)$ (from Patiño Douce [72]). (b) Molar $\text{Al}_2\text{O}_3/(\text{MgO} + \text{Fe}_2\text{O}_3^{\text{T}})$ versus molar $\text{CaO}/(\text{MgO} + \text{Fe}_2\text{O}_3^{\text{T}})$ (from Altherr [73]). (c) SiO_2 versus Mg# diagram (Mg# = molecular $\text{Mg}^{2+}/(\text{Mg}^{2+} + \text{Fe}^{2+})$) (from Rapp and Watson [71]). (d) Nb versus Nb/Th (primitive mantle data are after Hofmann [74], MORB + OIB and arc-type rocks fields are after Schmidberger and Hegner [75])

Furthermore, experimental petrology demonstrated that partial melting of mafic or basaltic lower crust could not produce high Mg-number ($\text{Mg}/(\text{Mg} + \text{TFe})$) magmas [71]. Therefore, high Mg-number magmas suggest injection of mantle-derived magma, excluding partial melting of the pure crust (Figure 9c). Moreover, the granite pluton shows an arc-type geochemical feature characterized by enrichment of light REE and Pb as well as Nb–Ta–Ti depletion (Figure 6a,b), demonstrating that the granite pluton originated from the recycling of arc-related rocks and preserved arc-related features. Although supra-crustal materials also display arc-type geochemical features, this possibility is precluded owing to mantle-like oxygen characteristics (Figure 5e,f). This is also supported by the Nb versus Nb/Th diagram (Figure 9d).

5.3. Mineral Fractional Crystallization

In Figure 10, TiO₂ and MgO demonstrate non-linear trends with the variations of SiO₂ contents, suggesting that mafic minerals (e.g., amphibole, pyroxene, and biotite) have a minor role in the magma evolution (Figure 10a,c). Although minor amounts of biotite were found in the thin sections and field exposures (Figure 2e), biotite is usually considered as volatile, representing a later magma evolution process. Na₂O, TFe₂O₃, Al₂O₃, and CaO showed good linear relations with SiO₂ ($R^2 > 0.5$) (Figure 10b,d–f). It is notable that Na₂O and Al₂O₃ showed decreasing trends with increasing SiO₂, suggesting plagioclase and alkali feldspar crystallization fractionation (Figure 10b,e). However, steady linear relations, as suggested by TFe₂O₃ and CaO, suggest the absence of basic feldspar and mafic minerals in the evolution process (Figure 10d,f). In Figure 11, trace element discrimination diagrams correspond well with the Harker diagrams (Figure 10). Figure 11a,b also suggests that the combination of K-feldspar and plagioclase played a key role in the granitic pluton during the magma evolution process. In addition, Figure 11c,d indicates monazite crystallization and fractionation. However, Zr/Hf ratios had consistent ratios, ranging from 39 to 42 (Table 4), suggesting that zircon fractional crystallization was negligible [76,77].

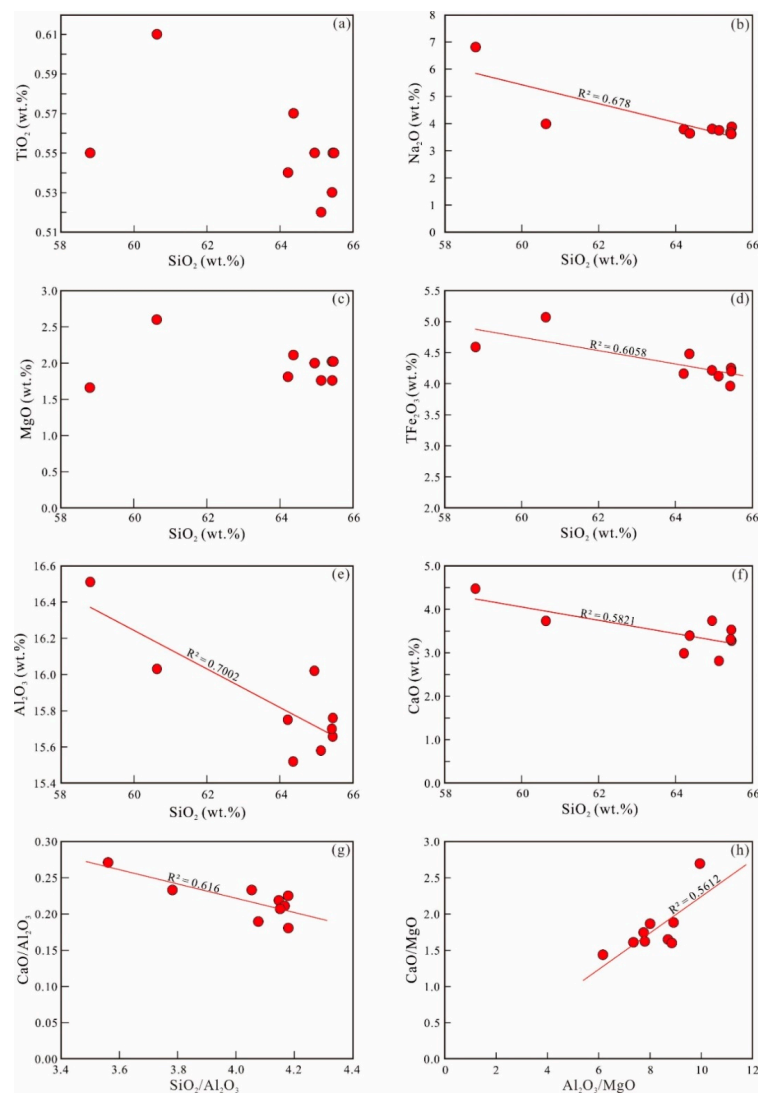


Figure 10. (a–f) Major elements versus SiO₂ Harker diagrams (red dot for the studied samples). (g,h) Diagrams of SiO₂/Al₂O₃ versus CaO/Al₂O₃ and Al₂O₃/MgO versus CaO/MgO (the magma mixing model is from Langmuir [78]).

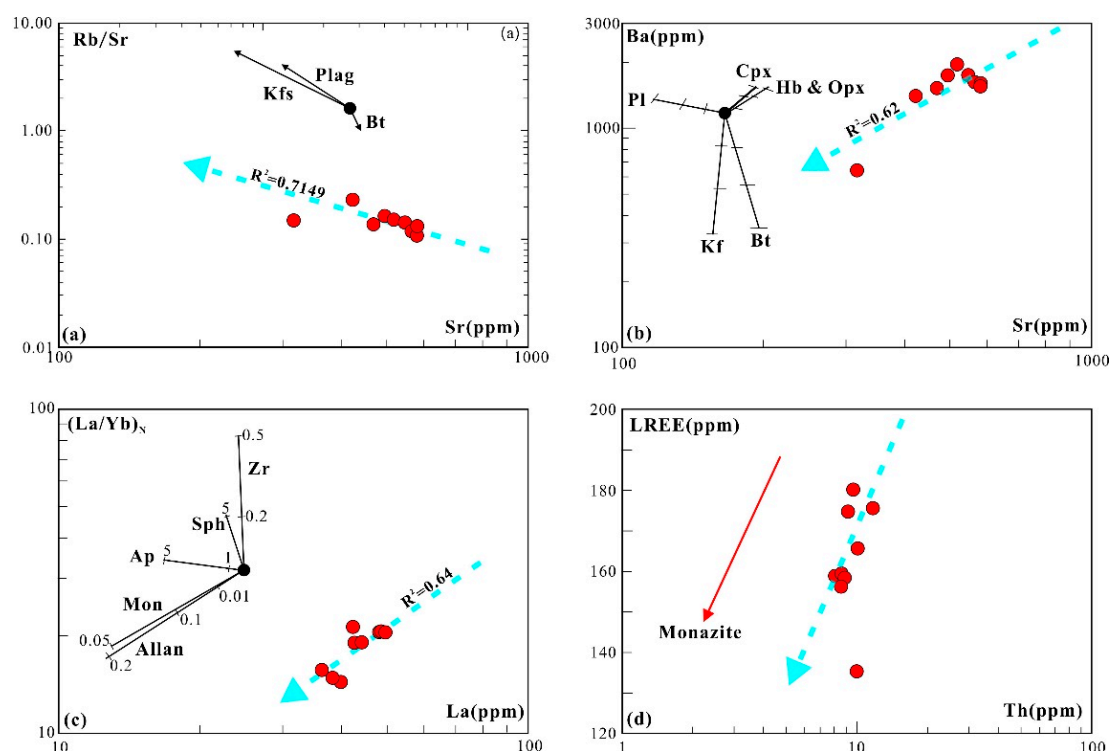


Figure 11. Mineral fractional evolution curves for the studied samples; (a,b) Sr versus Rb/Sr and Sr versus Ba diagrams (modeling curves are from Yang [2]). (c) La versus $(La/Yb)_N$; (d) Th versus LREE. Allan: allanite; Ap: apatite; Bt: biotite; Cpx: clinopyroxene; Hb: hornblende; Kfs or Kf: K-feldspar; Mon: monazite; Opx: orthopyroxene; Plag or Pl: plagioclase; Sph: sphene; Zr: zircon

5.4. Evaluation on the Adakite-Like Rocks

Previous studies revealed that Late Jurassic granites show high Sr/Y and $(La/Yb)_N$ ratios, suggesting that they originated from partial melting of thickened crust. As mentioned above, Early Cretaceous granites show complicated geochemical features. Some granitic plutons, distributed in northeastern segment of the Jiaodong peninsula, have high Sr/Y and $(La/Yb)_N$ ratios that are consistent with adakite-like rocks [79–81], whereas the other granites are characterized by low Sr/Y and $(La/Yb)_N$ ratios in the Sulu belt. Compared to the Late Jurassic adakite-like rocks, the petrogenesis and setting of the Early Cretaceous adakite-like rocks are poorly understood. In this study, our samples show arc-related geochemical characteristics (Figure 12a). However, the Yb_N versus $(La/Yb)_N$ diagram indicates an adakite-like feature corresponding to thickened crust (Figure 12b). It is well known that eastern China experienced significant lithospheric thinning and foundering [11,50,82], so it is untenable that the Early Cretaceous adakite-like rocks were formed in a thickened setting.

It has been attested that adakite-like rocks, as defined by Sr/Y and $(La/Yb)_N$ discriminant diagrams, can be formed in different settings: (1) Partial melting of thickened crust or foundering crust [83–85]; (2) Partial melting of the oceanic slab [86]; (3) Crystallization and differentiation [87,88]; (4) A high Sr/Y magma source [43]; (5) Magma mixing of different end-members [89,90]; and (6) Partial melting of granulite rocks [91]. It is generally accepted that (1) and (2) occur for true adakite rocks, while the other types (3 to 6) occur for pseudo-adakites [85,92]. He [93] proposed new discriminant diagrams that can better discriminate true and pseudo adakites. Figure 12c–f reveals that the samples plot into the normal granitic fields rather than normal genetic adakites. Combined with regional background and geochemical characteristics of early Cretaceous granites, we argue that early Cretaceous granites originated from partial melting of normal crustal material rather than thickened crust in the Sulu belt. However, our samples are characterized by high $(La/Yb)_N$ ratios that might be related to magma mixing, as suggested by magma mixing lines [78] (Figure 10g,h).

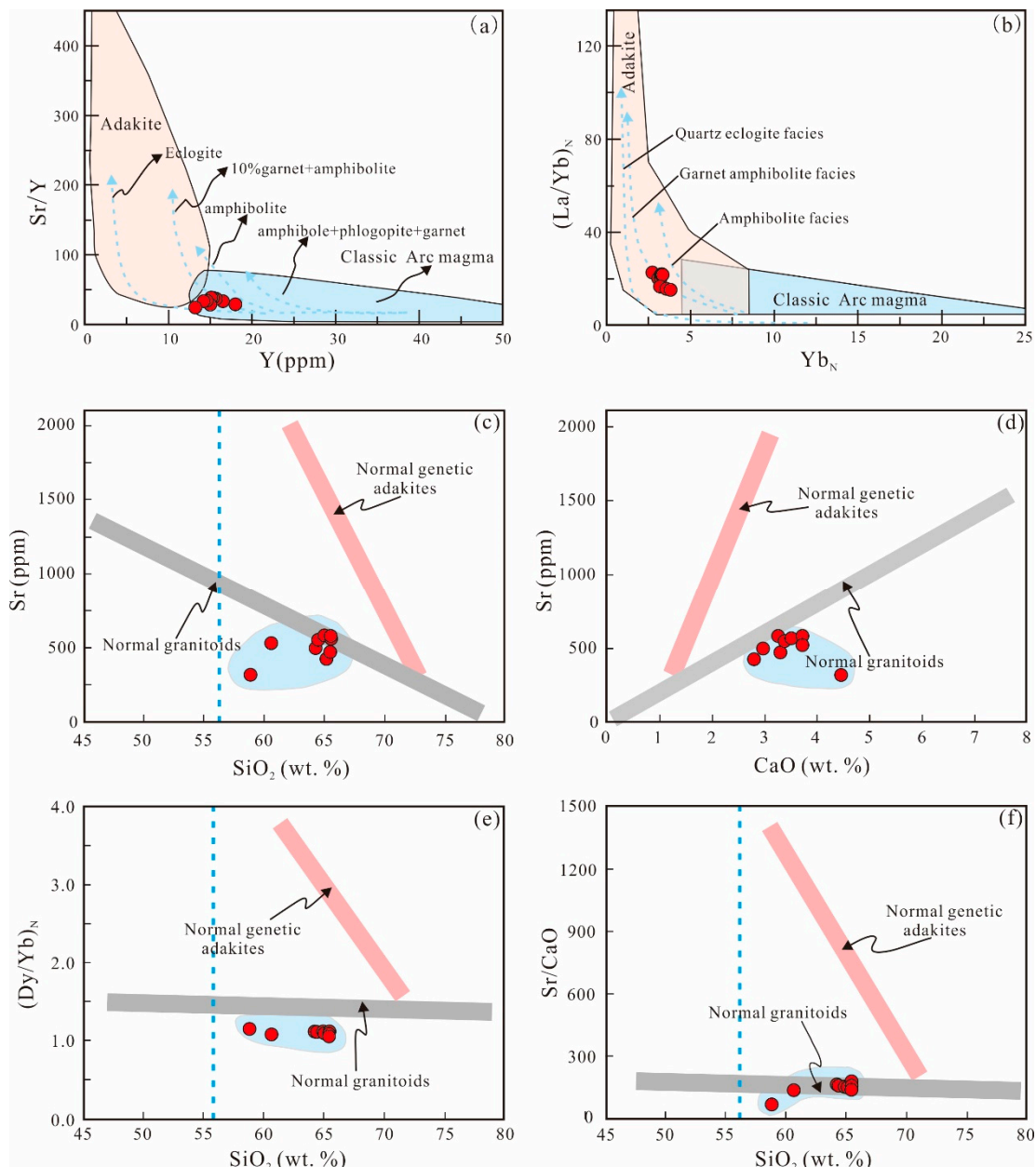


Figure 12. Discrimination diagrams for adakitic rocks (red dot for studied samples); (a,b) Y versus Sr/Y and Yb_N versus $(La/Yb)_N$ diagrams for adakite rocks (from Petford [83] and Defant [94]). (c) SiO_2 versus Sr. (d) CaO versus Sr. (e) SiO_2 versus $(Dy/Yb)_N$, (f) SiO_2 versus Sr/CaO (c–f are from He [93]).

5.5. Tectonic Implications

It is well known that underplating of mantle-derived, basaltic magma at the crust–mantle boundary might be an important mechanism for crustal growth and recycling [71,95]. The significantly negative $\epsilon_{Hf}(t)$ values indicate multiple crustal recycling for the studied pluton. It was also proved that mantle-derived material and basaltic magma supplied sufficient heat to result in partial melting of crust material at the crust–mantle boundary. During the interaction process, the mantle material probably participates in the formation of granitic rocks. Multiple studies have demonstrated that mafic microgranular enclaves (MME) and high-Mg-number granites reflect input and participation of mantle material [71,92].

MMEs and the high-Mg-number values (>40) reveal that the mantle material probably participated in the evolution of the granitic pluton in study area (Figures 2a–c and 9c). Multiple studies have shown

that formational processes of MMEs can be classified as follows: (1) fragments or xenoliths of mafic country rocks [96]; (2) refractory solid residues [97,98]; (3) early products from co-genetic magma or mafic mineral cumulates [99]; and (4) mixed mafic–felsic magmas in the chamber [92,100]. Compared to other models, mafic–felsic magmas mixing is the dominant model in producing high-Mg-number granites. Based on microtectonics and geochemical features, we argue that magma mixing is the best candidate for forming the granitic pluton with the MMEs in the Sulu belt.

Multiple studies have proven that the eastern China passed through significant lithosphere thinning during the Mesozoic. Rifted basins and multiple extensional tectonics (e.g., metamorphic core complex) are the shallow responses of the lithosphere thinning in eastern China [11,101,102]. In addition, Early Cretaceous large-scale mineralization and magmatic flare-up also suggest tectonic mechanism transfer during the Jurassic to Early Cretaceous [11,103]. The Late Jurassic granitoid rocks mainly originated from partial melting of pure crust material, with no significant mantle material input in the Sulu belt. However, the Early Cretaceous granitoid rocks have complex petrogenetic mechanisms, including pure crust-derived granitoids, crust–mantle mixing-derived granitoids, and large amounts of intermediate-mafic dykes. Particular rock assemblages and extensional tectonics suggest that eastern China experienced large-scale extension and thinning during the Early Cretaceous. Zhu [104] proposed that the Pacific plate subduction beneath the eastern China was the main factor causing lithosphere destruction and thinning of eastern China during the Early Cretaceous. Furthermore, Zhu [104] reported that the stagnant slab lying in the mantle transition zone resulted in an unsteady mantle flow (convective asthenosphere), leading to overlying lithosphere mantle thinning and destruction. Combined above field observations and geochemical and Hf–O isotopes, we propose that underplating of mantle-derived magma was the main factor leading to partial melting of the Yangtze mafic lower crust in the Sulu orogenic belt. During the evolution process, the mantle-derived magma also participated in the formation of the Caochang granitic pluton. Mantle-like $\delta^{18}\text{O}$ values reveal that the Caochang granitic pluton originated from a deep crustal setting, with no water–rock interaction and strong tectonic hot or cold events.

6. Concluding Remarks

(1) The new identified granitic pluton was crystallized during the Early Cretaceous (ca. 120 Ma), as suggested by zircon U–Pb dating.

(2) In-situ zircon Hf–O isotope data from the Caochang granitic pluton demonstrate a decoupling correlation of significant negative $\varepsilon_{\text{Hf}}(t)$ and mantle-like $\delta^{18}\text{O}$ values, suggesting a basaltic lower crust origin with no supra-crustal material input and water–rock interaction.

(3) High Mg-number values and mafic micro-granular enclaves suggest mantle material participation during the granitic magma evolution.

(4) In this study, the newly identified granitic pluton was the product of the destruction of the NCC. The NCC destruction resulted in decompression and mantle-derived magma upwelling that led to partial melting of Yangtze lower crust material, forming the Caochang granitic pluton.

Author Contributions: Y.M. carried out a detailed geological survey and wrote this manuscript; Z.W. provided ideas and experimental funds; B.G. made a contribution to tectonic models and geochemical discrimination diagrams; J.L. made a contribution to experimental measurements and data processing. All authors have read and agreed to the published version of the manuscript.

Funding: This work was funded by the Young innovative projects of Shandong Province (2019KJH004), the National Natural Science Foundation of China (41902230, 41876059), and the Shandong Provincial Natural Science Foundation (ZR2019QD002).

Conflicts of Interest: The authors declare no conflict of interest.

References

1. Yang, J.H.; Chung, S.L.; Wilde, S.A.; Wu, F.Y.; Chu, M.F.; Lo, Q.H.; Fan, H.R. Petrogenesis of post-orogenic syenites in the Sulu Orogenic Belt, East China: Geochronological, geochemical and Nd-Sr isotopic evidence. *Chem. Geol.* **2005**, *214*, 99–125. [[CrossRef](#)]
2. Yang, J.H.; Wu, F.Y.; Chung, S.L.; Wilde, S.A.; Chu, M.F.; Lo, C.H.; Song, B. Petrogenesis of Early Cretaceous intrusions in the Sulu ultrahigh-pressure orogenic belt, East China and their relationship to lithospheric thinning. *Chem. Geol.* **2005**, *222*, 200–231. [[CrossRef](#)]
3. Liu, F.L.; Liu, L.S.; Liu, P.H.; Wang, F.; Cai, J.; Liu, J.H.; Wang, W.; Ji, L. A relic slice of Archean-early Paleoproterozoic basement of Jiaobei Terrane identified within the Sulu UHP belt: Evidence from protolith and metamorphic ages from meta-mafic rocks, TTG-granitic gneisses, and metasedimentary rocks in the Haiyangsuo region. *Precambrian Res.* **2017**, *303*, 117–152. [[CrossRef](#)]
4. Zhao, Z.F.; Liu, Z.B.; Chen, Q. Melting of subducted continental crust: Geochemical evidence from Mesozoic granitoids in the Dabie-Sulu orogenic belt, east-central China. *J. Asian Earth Sci.* **2017**, *145*, 260–277. [[CrossRef](#)]
5. Zhao, Z.F.; Zheng, Y.F. Remelting of subducted continental lithosphere: Petrogenesis of Mesozoic magmatic rocks in the Dabie-Sulu orogenic belt. *Sci. China Ser. D* **2009**, *52*, 1295–1318. [[CrossRef](#)]
6. Xu, Y.; Yang, M.L.; Polat, A.; Yang, K.G.; Meng, Y.K.; Li, R.H.; Wang, Z.B. Zircon U-Pb ages and Hf isotopic compositions of two types of supracrustal rocks in the Northeastern Sulu UHP terrane: Constraints on the surface boundary between South China and North China. *Int. Geol. Rev.* **2018**, *61*, 539–561. [[CrossRef](#)]
7. Wang, S.J.; Schertl, H.P.; Pang, Y.M. Geochemistry, geochronology and Sr-Nd-Hf isotopes of two types of early Cretaceous granite porphyry dykes in the Sulu Orogenic Belt, Eastern China. *Can. J. Earth Sci.* **2019**, *57*, 249–266. [[CrossRef](#)]
8. Zheng, Y.F. A perspective view on ultrahigh-pressure metamorphism and continental collision in the Dabie-Sulu orogenic belt. *Chin. Sci. Bull.* **2008**, *53*, 3081–3104. [[CrossRef](#)]
9. Liou, J.G.; Ernst, W.G.; Zhang, R.Y.; Tsujimori, T.; Jahn, B.M. Ultrahigh-pressure minerals and metamorphic terranes—the view from China. *J. Asian Earth Sci.* **2009**, *35*, 199–231. [[CrossRef](#)]
10. Zheng, Y.F.; Fu, B.; Gong, B.; Li, L. Stable isotope geochemistry of ultrahigh pressure metamorphic rocks from the Dabie–Sulu orogeny in China: Implications for geodynamics and fluid regime. *Earth Sci. Rev.* **2003**, *62*, 105–161. [[CrossRef](#)]
11. Meng, Y.K.; Santosh, M.; Li, R.H.; Xu, Y.; Hou, F.H. Petrogenesis and tectonic implications of Early Cretaceous volcanic rocks from Lingshan Island in the Sulu Orogenic Belt. *Lithos* **2018**, *312–313*, 244–257. [[CrossRef](#)]
12. Wang, H.; Wang, S.H.; Xu, Z.W.; Fu, B.; Zhao, Z.X.; Li, Z.G.; Dong, Y.H.; Tang, L.M.; Li, J. Geochemical and Sr-Nd-Pb-Hf-O isotopic compositions of the Tiezhai complex: Implications for lithosphere destruction of the North China Craton. *Gondwana Res.* **2018**, *61*, 203–221. [[CrossRef](#)]
13. Wang, J.; Chang, S.C.; Chen, Y.; Yan, S.Y. Early Cretaceous transpressional and transtensional tectonics straddling the Sulu orogenic belt, East China. *Geosci. Front.* **2019**, *10*, 2287–2300. [[CrossRef](#)]
14. Xu, H.J.; Zhang, J.F.; Wang, Y.F.; Liu, W.L. Late Triassic alkaline complex in the Sulu UHP terrane: Implication for post-collisional magmatism and subsequent fractional crystallization. *Gondwana Res.* **2016**, *35*, 390–410. [[CrossRef](#)]
15. Zhao, Z.F.; Zheng, Y.F.; Zhang, J.; Dai, L.Q.; Liu, X.M. Syn-exhumation magmatism during continental collision: Evidence from alkaline intrusives of Triassic age in the Sulu orogen. *Chem. Geol.* **2012**, *328*, 70–88. [[CrossRef](#)]
16. Jahn, B.M.; Wu, F.Y.; Lo, C.H.; Tsai, C.H. Crust-mantle interaction induced by deep subduction of the continental crust: Geochemical and Sr-Nd isotopic evidence from post-collisional mafic-ultramafic intrusions of the northern Dabie complex, central China. *Chem. Geol.* **1999**, *157*, 119–146. [[CrossRef](#)]
17. Zhou, X.M.; Li, W.X. Origin of Late Mesozoic igneous rocks of southeastern China: Implications for lithosphere subduction and underplating of mafic magma. *Tectonophysics* **2000**, *326*, 269–287. [[CrossRef](#)]
18. Zhao, Z.F.; Zheng, Y.F.; Chen, Y.X.; Sun, G.C. Partial melting of subducted continental crust: Geochemical evidence from synexhumation granite in the Sulu orogen. *Geol. Soc. Am. Bull.* **2017**, *129*, 1692–1707. [[CrossRef](#)]
19. Niu, Y.L.; Liu, Y.; Xue, Q.Q.; Shao, F.L.; Chen, S.; Duan, M.; Guo, P.Y.; Gong, H.M.; Hu, Y.; Hu, Z.X.; et al. The exotic origin of the continental shelf of East and South China Seas—a testable hypothesis with consequences on the tectonic evolution of the western Pacific and eastern China since the Mesozoic. *Sci. Bull.* **2015**, *18*, 1598–1616. [[CrossRef](#)]

20. Gao, Y.J.; Niu, Y.L.; Duan, M.; Xue, Q.Q.; Sun, P.; Chen, S.; Xiao, Y.Y.; Guo, P.Y.; Wang, X.H.; Chen, Y.H. The petrogenesis and tectonic significance of the Early Cretaceous intraplate granites in eastern China: The Laoshan granite as an example. *Lithos* **2019**, *328–329*, 200–211. [[CrossRef](#)]
21. Dai, L.Q.; Zheng, Y.F.; Zhao, Z.F. Termination time of peak decratonization in North China: Geochemical evidence from mafic igneous rocks. *Lithos* **2016**, *240–243*, 327–336. [[CrossRef](#)]
22. Ling, M.X.; Li, Y.; Ding, X.; Teng, F.Z.; Yang, X.Y.; Fan, W.M.; Xu, Y.G.; Sun, W.D. Destruction of the North China Craton induced by ridge subductions. *J. Geol.* **2013**, *121*, 197–213. [[CrossRef](#)]
23. Yan, Q.S.; Shi, X.F. Geochemistry and petrogenesis of the Cretaceous A-type granites in the Laoshan granitic complex, eastern China. *Island Arc* **2014**, *23*, 221–235. [[CrossRef](#)]
24. Zhang, J.; Zhao, Z.F.; Zheng, Y.F.; Dai, M.N. Postcollisional magmatism: Geochemical constraints on the petrogenesis of Mesozoic granitoids in the Sulu orogen, China. *Lithos* **2010**, *119*, 512–536. [[CrossRef](#)]
25. Zhang, J.; Zhao, Z.F.; Zheng, Y.F.; Liu, X.M.; Xie, L.W. Zircon Hf–O isotope and whole-rock geochemical constraints on origin of postcollisional mafic to felsic dykes in the Sulu orogen. *Lithos* **2012**, *136*, 225–245. [[CrossRef](#)]
26. Meng, Y.K.; Li, R.H.; Xu, Y.; Hou, F.H. U–Pb–Hf isotopes and tectonic significance of early Cretaceous detrital zircons on Lingshan Island, Qingdao of Shandong Province. *Earth Sci.* **2018**, *43*, 3302–3323.
27. Zhou, J.B.; Wilde, S.A.; Zhao, G.C.; Zhang, X.Z.; Zheng, C.Q.; Jin, W.; Cheng, H. SHRIMP U–Pb zircon dating of the Wulian complex: Defining the boundary between the north and south China cratons in the Sulu orogenic belt, China. *Precambrian Res.* **2008**, *162*, 559–576. [[CrossRef](#)]
28. Zhou, J.B.; Wilde, S.; Zhao, G.C.; Zheng, C.Q.; Jin, W.; Zhang, X.Z.; Cheng, H. SHRIMP U–Pb zircon dating of the Neoproterozoic Penglai Group and Archean gneisses from the Jiaobei terrane, north China, and their tectonic implications. *Precambrian Res.* **2008**, *160*, 323–340. [[CrossRef](#)]
29. Guo, J.H.; Chen, F.K.; Zhang, X.M.; Siebel, W.; Zhai, M.G. Evolution of syn- to post-collisional magmatism from north Sulu UHP belt, eastern China: Zircon U–Pb geochronology. *Acta Petrol. Sin.* **2005**, *21*, 1281–1301.
30. Liu, Y.S.; Hu, Z.C.; Zong, K.Q.; Gao, C.G.; Gao, S.; Xu, J.; Chen, H.H. Reappraisal and refinement of zircon U–Pb isotope and trace element analyses by LA-ICP-MS. *Chin. Sci. Bull.* **2010**, *55*, 1535–1546. [[CrossRef](#)]
31. Zong, K.Q.; Liu, Y.S.; Gao, C.G.; Hu, Z.H.; Gao, S.; Gong, H.J. In situ U–Pb dating and trace element analysis of zircons in thin sections of eclogite: Refining constraints on the UHP metamorphism of the Sulu terrane, China. *Chem. Geol.* **2010**, *269*, 237–251. [[CrossRef](#)]
32. Williams, I.S. U–Th–Pb geochronology by ion microprobe. In *Applications of Microanalytical Techniques to Understanding Mineralizing Processes*; McKibben, M.A., Shanks, W.C., Ridley, W.I., Eds.; Review of Economic Geology; Society of Economic Geologists: Littleton, CO, USA, 1998; Volume 7, pp. 1–35.
33. Black, L.P.; Kamo, S.L.; Allen, C.M.; Davis, D.W.; Aleinikoff, J.N.; Valley, J.W.; Mundil, R.; Campbell, I.H.; Korsch, R.J.; Williams, I.S.; et al. Improved $^{206}\text{Pb}/^{238}\text{U}$ microprobe geochronology by the monitoring of a trace-element related matrix effect; SHRIMP, ID-TIMS, ELA-ICP-MS and oxygen isotope documentation for a series of zircon standards. *Chem. Geol.* **2004**, *205*, 115–140. [[CrossRef](#)]
34. Hu, Z.C.; Liu, Y.S.; Gao, S.; Liu, W.G.; Yang, L.; Zhang, W.; Tong, X.R.; Lin, L.; Zong, K.Q.; Li, M.; et al. Improved in situ Hf isotope ratio analysis of zircon using newly designed X skimmer cone and Jet sample cone in combination with the addition of nitrogen by laser ablation multiple collector ICP-MS. *J. Anal. At. Spectrom.* **2012**, *27*, 1391–1399. [[CrossRef](#)]
35. Hoskin, P.W.O.; Schaltegger, U. The composition of zircon and igneous and metamorphic petrogenesis. *Rev. Mineral. Geochem.* **2003**, *53*, 27–62. [[CrossRef](#)]
36. Andersen, T. Correction of common lead in U–Pb analyses that do not report ^{204}Pb . *Chem. Geol.* **2002**, *192*, 59–79. [[CrossRef](#)]
37. Xiong, F.H.; Meng, Y.K.; Yang, J.S.; Liu, Z.; Xu, X.Z.; Eslami, A.; Zhang, R. Geochronology and petrogenesis of the mafic dykes from the Purang ophiolite: Implications for evolution of the western Yarlung–Tsangpo suture zone, Tibet. *Geosci. Front.* **2020**, *11*, 277–292. [[CrossRef](#)]
38. Middlemost, E.A.K. Naming materials in the magma/igneous rock system. *Earth-Sci. Rev.* **1994**, *37*, 215–224. [[CrossRef](#)]
39. Irvine, T.N.; Baragar, W.R.A. A guide to the chemical classification of the common volcanic rocks. *Can. J. Earth Sci.* **1971**, *8*, 523–548. [[CrossRef](#)]
40. Wright, J.B. A simple alkalinity ratio and its application to questions of non-orogenic granite genesis. *Geol. Mag.* **1969**, *106*, 370–384. [[CrossRef](#)]

41. Peccerillo, A.; Taylor, S.R. Geochemistry of Eocene calc-alkaline volcanic rocks from the Kastamonu area, northern Turkey. *Contrib. Miner. Petrol.* **1976**, *58*, 63–81. [[CrossRef](#)]
42. Maniar, P.D.; Piccoli, P.M. Tectonic discrimination of granitoids. *Geol. Soc. Am. Bull.* **1989**, *101*, 635–643. [[CrossRef](#)]
43. Moyen, J.F. High Sr/Y and La/Yb ratios: The meaning of the adakitic signature. *Lithos* **2009**, *112*, 556–574. [[CrossRef](#)]
44. Sun, T.; Zhou, X.M.; Chen, P.R.; Li, H.M.; Zhou, H.Y.; Wang, Z.C.; Shen, W.Z. Mesozoic strong peraluminous granite and its tectonic significance in the eastern Nanling Mountains, China. *Sci. China Ser. D* **2003**, *33*, 1209–1218.
45. Boynton, W.V. Geochemistry of the rare earth elements: Meteorite studies. In *Rare Earth Element Geochemistry*; Henderson, P., Ed.; Elsevier: Amsterdam, The Netherlands, 1984; pp. 63–114.
46. Sun, S.S.; McDonough, W.F. Chemical and isotopic systematics of oceanic basalts: Implications for mantle composition and processes. In *Magmatism in the Ocean Basins*; Saunders, A.D., Norry, M.J., Eds.; Geological Society of London Special Publications: London, UK, 1989; Volume 42, pp. 313–345.
47. Chappell, B.W.; White, A.J.R. Two contrasting granite types. *Pac. Geol.* **1974**, *8*, 173–174.
48. Loiselle, M.C.; Wones, D.R. Characteristics and origin of anorogenic granites. *Geol. Soc. Am. Abstr.* **1979**, *11*, 468.
49. Hao, L.L.; Wang, Q.; Wyman, D.A.; Ma, L.; Wang, J.; Xia, X.P.; Qu, Q. First identification of postcollisional A-type magmatism in the Himalayan-Tibetan orogen. *Geology* **2019**, *47*, 187–190. [[CrossRef](#)]
50. Zhu, R.X.; Yang, J.H.; Wu, F.Y. Timing of destruction of the North China Craton. *Lithos* **2012**, *149*, 51–60. [[CrossRef](#)]
51. Watson, E.B.; Wark, D.A.; Thomas, J.B. Crystallization thermometers for zircon and rutile. *Contrib. Mineral. Petrol.* **2006**, *151*, 413–433. [[CrossRef](#)]
52. Zhao, G.T.; Wang, D.Z.; Cao, Q.C. The geochemistry and genesis of the Laoshan Granitoids, Shandong Province. *Geol. J. China Univ.* **1997**, *3*, 1–15.
53. Whalen, J.B.; Currie, K.L.; Chappell, B.W. A-type granites: Geochemical characteristics, discrimination and petrogenesis. *Contrib. Miner. Petrol.* **1987**, *95*, 407–419. [[CrossRef](#)]
54. Chappell, B.W.; White, A.J.R. I- and S-type granites in the Lachlan Fold Belt. *Transactions of the Royal Society of Edinburgh: Earth Sci.* **1992**, *83*, 1–26. [[CrossRef](#)]
55. Chappell, B.W. Aluminium saturation in I- and S-type granites and the characterization of fractionated haplogranites. *Lithos* **1999**, *46*, 535–551. [[CrossRef](#)]
56. Zhang, S.B.; Zheng, Y.F. Time and space of Neoproterozoic low $\delta^{18}\text{O}$ magmatic rocks in South China. *Chin. Sci. Bull.* **2013**, *58*, 2344–2350.
57. Gao, P.; Zheng, Y.F.; Zhao, Z.F. Distinction between S-type and peraluminous I-type granites: Zircon versus whole-rock geochemistry. *Lithos* **2016**, *258*, 77–91. [[CrossRef](#)]
58. Lu, Y.H.; Gao, P.; Zhao, Z.F.; Zheng, Y.F. Whole-rock geochemical and zircon Hf-O isotopic constraints on the origin of granitoids and their mafic enclaves from the Triassic Mishuling pluton in West Qinling, central China. *J. Asian Earth Sci.* **2019**, *189*, 104136. [[CrossRef](#)]
59. Zhao, R.; Wang, Q.F.; Liu, X.F.; Wang, W.; Pan, R.G. Architecture of the Sulu crustal suture between the North China Craton and Yangtze Craton: Constraints from Mesozoic granitoids. *Lithos* **2016**, *266*, 348–361. [[CrossRef](#)]
60. Wu, F.Y.; Li, X.H.; Zheng, Y.F.; Gao, S. Lu-Hf isotopic systematics and their applications in petrology. *Acta Petrol. Sin.* **2007**, *23*, 185–220.
61. Griffin, W.L.; Wang, X.; Jackson, S.E.; Pearson, N.J.; O'Reilly, S.Y.; Xu, X.; Zhou, X. Zircon chemistry and magmamixing, SE China: In-situ analysis of Hf isotopes, Tonglu and Pingtan igneous complexes. *Lithos* **2002**, *61*, 237–269. [[CrossRef](#)]
62. Dawson, J.B.; Carswell, D.A.; Hall, J.; Wedepohl, K.H. *The nature of the Lower Continental Crust*; Geological Society Special Publication: London, UK, 1986; Volume 24, pp. 363–374.
63. Rudnick, R.L.; Gao, S. Composition of the continental crust. *Treatise Geochem.* **2003**, *3*, 1–64.
64. Valley, J.W.; Lackey, J.S.; Cavosie, A.J.; Clechenko, C.C.; Spicuzza, M.J.; Basei, M.A.S.; Bindeman, I.N.; Ferreira, V.P.; Sial, A.N.; King, E.M.; et al. 4.4 billion years of crustal maturation: Oxygen isotope ratios of magmatic zircon. *Contrib. Mineral. Petrol.* **2005**, *150*, 561–580. [[CrossRef](#)]

65. Ma, Q.; Xu, Y.G.; Huang, X.L.; Zheng, J.P.; Ping, X.Q.; Xia, X.P. Eoarchean to Paleoproterozoic crustal evolution in the North China Craton: Evidence from U-Pb and Hf-O isotopes of zircons from deep-crustal xenoliths. *Geochimica et Cosmochimica Acta*. **2019**, *278*, 94–109. [[CrossRef](#)]
66. Kemp, A.I.S.; Hawkesworth, C.J.; Foster, G.L.; Paterson, B.A.; Woodhead, J.D.; Hergt, J.M.; Gray, C.M.; Whitehouse, M.J. Magmatic and crustal differentiation history of granitic rocks from Hf-O isotopes in zircon. *Science* **2007**, *315*, 980–983. [[CrossRef](#)]
67. Gao, S.; Yang, J.; Zhou, L.; Li, M.; Hu, Z.; Guo, J.; Yuan, H.; Gong, H.; Xiao, G.; Wei, J. Age and growth of the Archean Kongling terrain, South China, with Emphasis on 3.3 Ga granitoid gneisses. *Am. J. Sci.* **2011**, *311*, 153–182. [[CrossRef](#)]
68. Guo, J.L.; Wu, Y.B.; Gao, S.; Jin, Z.M.; Zong, K.Q.; Hu, Z.C.; Chen, K.; Chen, H.H.; Liu, Y.S. Episodic Paleoproterozoic-Paleoproterozoic (3.3–2.0 Ga) granitoid magmatism in Yangtze craton, South China: Implications for Late Archean Tectonics. *Precambrian Res.* **2015**, *270*, 246–266. [[CrossRef](#)]
69. Taylor, S.R.; Campbell, I.H.; McCulloch, M.T.; McLennan, S.M. A lower crustal origin for massif-type anorthosites. *Nature* **1984**, *311*, 372. [[CrossRef](#)]
70. He, H.L.; Song, X.Y.; Zhai, M.G.; Yu, S.Y.; Du, Z.S. Lower crustal contribution to the magma formation of the Damiao massif-type anorthosite, North China Craton: Evidence from zircon Hf-O isotopes. *Precambrian Res.* **2019**, *332*, 105396. [[CrossRef](#)]
71. Rapp, R.P.; Watson, E.B. Dehydration melting of metabasalt at 8–32 kbar: Implications for continental growth and crust-mantle recycling. *J. Petrol.* **1995**, *36*, 891–931. [[CrossRef](#)]
72. Patiño Douce, A.E. What do experiments tell us about the relative contributions of crust and mantle to the origin of granitic magmas? In *Understanding Granites: Intergrating New and Classical Techniques*; Castro, A., Fernandez, C., Vigneresse, J.L., Eds.; Special Publications, Geological Society London: London, UK, 1999; Volume 168, pp. 55–75.
73. Altherr, R.; Holl, A.; Hegner, E. High-potassium, calc-alkaline I-type plutonism in the European Variscides: Northern Vosges (France) and northern Schwarzwald (Germany). *Lithos* **2000**, *50*, 51–73. [[CrossRef](#)]
74. Hofmann, A.W. Chemical differentiation of the Earth: The relationship between mantle, continental crust, and oceanic crust. *Earth Planet. Sci. Lett.* **1988**, *90*, 297–314. [[CrossRef](#)]
75. Schmidberger, S.S.; Hegner, E. Geochemistry and isotope systematics of calc-alkaline volcanic rocks from the Saar-Nahe basin (SW Germany): Implications for Late-Variscan orogenic development. *Contrib. Mineral. Petrol.* **1999**, *135*, 373–385. [[CrossRef](#)]
76. Dostal, J.; Chatterjee, A.K. Contrasting behaviour of Nb/Ta and Zr/Hf ratios in a peraluminous granitic pluton (Nova Scotia, Canada). *Chem. Geol.* **2000**, *163*, 207–218. [[CrossRef](#)]
77. Linnen, R.L.; Keppler, H. Columbite solubility in granitic melts: Consequence for the enrichment and fractionation of Nb and Ta in the Earth's crust. *Contrib. Mineral. Petrol.* **1997**, *128*, 213–227. [[CrossRef](#)]
78. Langmuir, C.H.; Vocke, R.D.; Hanson, G.N.; Hart, S.R. A general mixing equation with applications to Icelandic basalts. *Earth Planet. Sci. Lett.* **1978**, *37*, 380–392. [[CrossRef](#)]
79. Yang, J.H.; Zhu, M.F.; Liu, W.; Zhai, M.G. Geochemistry and petrogenesis of Guojialing granodiorites from the northwestern Jiaodong Peninsula, eastern China. *Acta Petrol. Sin.* **2003**, *19*, 692–700.
80. Zhang, H.F.; Zhai, M.G.; Tong, Y.; Peng, P.; Xu, B.L.; Guo, J.H. Petrogenesis of the Sanfoshan high-Ba-Sr granite, Jiaodong Peninsula, eastern China. *Geol. Rev.* **2006**, *52*, 43–53.
81. Du, L.; Zhang, Y.Y.; Huang, Z.Y.; Li, X.-P.; Yuan, C.; Wu, B.; Long, X.P. Devonian to Carboniferous tectonic evolution of the Kangguer Ocean in the Eastern Tianshan, NW China: Insights from three episodes of granitoids. *Lithos* **2019**, *350*, 105243. [[CrossRef](#)]
82. Liu, J.G.; Cai, R.H.; Pearson, D.G.; Scott, J.M. Thinning and destruction of the lithospheric mantle root beneath the North China Craton: A review. *Earth Sci. Rev.* **2019**, *196*, 102873. [[CrossRef](#)]
83. Petford, N.; Atherton, M. Na-rich partial melts from newly underplated basaltic crust: The Cordillera Blanca Batholith. *Peru. J. Petrol.* **1996**, *37*, 1491–1521. [[CrossRef](#)]
84. Xu, J.F.; Shinjo, R.; Defant, M.J.; Wang, Q.; Rapp, R.P. Origin of Mesozoic adakitic intrusive rocks in the Ningzhen area of east China: Partialmelting of delaminated lower continental crust? *Geology* **2002**, *30*, 1111–1114. [[CrossRef](#)]
85. Xu, H.J.; Ma, C.Q.; Ye, K. Early cretaceous granitoids and their implications for the collapse of the Dabie orogen, eastern China: SHRIMP zircon U-Pb dating and geochemistry. *Chem. Geol.* **2007**, *240*, 238–259. [[CrossRef](#)]

86. Defant, M.J.; Drummond, M.S. Derivation of some modern arc magmas by melting of young subducted lithosphere. *Nature* **1990**, *347*, 662–665. [[CrossRef](#)]
87. Richards, J.P.; Kerrich, R. Adakite-like rocks: Their diverse origins and questionable role in metallogenesis. *Econ. Geol.* **2007**, *102*, 537–576. [[CrossRef](#)]
88. Xu, W.C.; Zhang, H.F.; Luo, B.J.; Guo, L.; Yang, H. Adakite-like geochemical signature produced by amphibole-dominated fractionation of arc magmas: An example from the Late Cretaceous magmatism in Gangdese belt, southern Tibet. *Lithos* **2015**, *232*, 197–210. [[CrossRef](#)]
89. Chen, B.; Jahn, B.M.; Arakawa, Y.; Zhai, M.G. Petrogenesis of the Mesozoic intrusive complexes from the southern Taihang Orogen, North China Craton: Elemental and Sr-Nd-Pb isotopic constraints. *Contrib. Mineral. Petrol.* **2004**, *148*, 489–501. [[CrossRef](#)]
90. Guo, F.; Nakamura, E.; Fan, W.M.; Kobayoshi, K.; Li, C.W. Generation of Palaeocene adakitic andesites by magma mixing; Yanji Area, NE China. *J. Petrol.* **2007**, *48*, 661–692. [[CrossRef](#)]
91. Jiang, N.; Liu, Y.S.; Zhou, W.G.; Yang, J.H.; Zhang, S.Q. Derivation of Mesozoic adakitic magmas from ancient lower crust in the North China craton. *Geochim. Cosmochim. Acta* **2007**, *71*, 2591–2608. [[CrossRef](#)]
92. Meng, Y.K.; Xiong, F.H.; Xu, Z.Q.; Ma, X.X. Petrogenesis of Late Cretaceous mafic enclaves and their host granites in the Nyemo region of southern Tibet: Implications for the tectonic-magmatic evolution of the Central Gangdese Belt. *J. Asian Earth Sci.* **2019**, *176*, 27–41. [[CrossRef](#)]
93. He, Y.S.; Li, S.G.; Hoefs, J.; Huang, F.; Liu, S.A.; Hou, Z.H. Post-collisional granitoids from the Dabie orogen: New evidence for partial melting of thickened continental crust. *Geochim. Cosmochim. Acta* **2011**, *75*, 3815–3838. [[CrossRef](#)]
94. Defant, M.; Xu, J.; Kepezhinskas, P.; Wang, Q.; Zhang, Q.; Xiao, L.; Defant, M. Adakites: Some variations on a theme. *Acta Petrol. Sin.* **2002**, *18*, 129–142.
95. Rudnick, R. Growing from below. *Nature* **1990**, *347*, 711–712. [[CrossRef](#)]
96. Maas, R.; Nicholls, I.A.; Legg, C. Igneous and metamorphic enclaves in the S-type Deddick granodiorite, Lachlan Fold Belt, SE Australia: Petrographic, geochemical and Nd-Sr isotopic evidence for crustal melting and magma mixing. *J. Petrol.* **1997**, *38*, 815–841. [[CrossRef](#)]
97. White, R.V.; Tarney, J.; Kerr, A.C.; Saunders, A.D.; Kempton, P.D.; Pringle, M.S.; Klaver, G.T. Modification of an oceanic plateau, Aruba. Dutch Caribbean: Implications for the generation of continental crust. *Lithos* **1999**, *46*, 43–68. [[CrossRef](#)]
98. Kazemi, K.; Kananian, A.; Xiao, Y.L.; Sarjoughian, F. Petrogenesis of Middle-Eocene granitoids and their mafic microgranular enclaves in central Urmia-Dokhtar Magmatic Arc (Iran): Evidence for interaction between felsic and mafic magmas. *Geosci. Front.* **2018**, *10*, 705–723. [[CrossRef](#)]
99. Shellnutt, J.G.; Jahn, B.M.; Dostal, J. Elemental and Sr-Nd isotope geochemistry of microgranular enclaves from peralkaline A-type granitic plutons of the Emeishan large igneous province, SW China. *Lithos* **2010**, *119*, 34–46. [[CrossRef](#)]
100. Barbarin, B. Mafic magmatic enclaves and mafic rocks associated with some granitoids of the central Sierra Nevada batholith, California: Nature, origin, and relations with the hosts. *Lithos* **2005**, *88*, 155–177. [[CrossRef](#)]
101. Charles, N.; Gumiaux, C.; Augier, R.; Chen, Y.; Zhu, R.; Lin, W. Metamorphic core complexes vs. synkinematic plutons in continental extension setting: Insights from key structures (Shandong Province, eastern China). *J. Asian Earth Sci.* **2011**, *40*, 261–278. [[CrossRef](#)]
102. Charles, N.; Augier, R.; Gumiaux, C.; Monié, P.; Chen, Y.; Faure, M.; Zhu, R. Timing, duration and role of magmatism in wide rift systems: Insights from the Jiaodong Peninsula (China, East Asia). *Gondwana Res.* **2013**, *24*, 412–428. [[CrossRef](#)]
103. Wang, J.; Chang, S.C.; Wang, K.L.; Lu, H.B.; Zhang, H.C. Geochronology and geochemistry of early cretaceous igneous units from the central Sulu orogenic belt: Evidence for crustal delamination during a shift in the regional tectonic regime. *J. Asian Earth Sci.* **2015**, *112*, 49–59. [[CrossRef](#)]
104. Zhu, R.X.; Xu, Y.G. The subduction of the west Pacific plate and the destruction of the north China craton. *Sci. China Earth Sci.* **2019**, *62*, 1340–1350. [[CrossRef](#)]

